THE STUDY OF NEUTRON-RICH NUCLEI, ^{9}LI AND ^{13}BE, THROUGH ISOBARIC ANALOGUE STATES USING RESONANT SCATTERING

A Dissertation

by

CURTIS NATHANIEL HUNT

Submitted to the Graduate and Professional School of
Texas A&M University
in partial fulfillment of the requirements for the degree of

DOCTOR OF PHILOSOPHY

Chair of Committee,	Grigory V. Rogachev
Committee Members,	Charles M. Folden III
	Jeremy W. Holt
	Dan G. Melconian
Head of Department,	Grigory V. Rogachev

May 2022

Major Subject: Physics

ABSTRACT

The development of a unified approach in nuclear theory, which starts from bare nucleon-nucleon and multi-nucleon forces and makes accurate predictions on the structure of atomic nuclei is a major goal of modern nuclear physics. A truly breakneck speed of theoretical advances in this area during the last three decades, coupled with modern computational techniques and hardware, has produced an array of new theoretical models, capable of making robust *ab initio* predictions for nuclear systems with an ever-growing number of nucleons. Comprehensive and multifaceted experimental tests of these models are indispensable. Light exotic nuclei are particularly important for these tests due to a combination of several factors. *Ab initio* calculations are more manageable for light nuclei (few nucleons). Exotic nuclei by definition have an imbalance between protons and neutrons, adding an isospin dimension to the tests. Small (or negative) binding energies of exotic nuclei make the effects of the continuum more important even for the lowest or ground states, adding yet another important factor to the model tests. Finally, exotic nuclei are known to often have unusual structures with experimentally observed or observable signatures, such as neutron halos, and we expect the *ab initio* models to reproduce these new features.

A method of studying the structure of exotic, neutron-rich nuclei by populating the corresponding isobaric analogue states in less exotic isobaric partners is discussed in this thesis. It is benchmarked for the relatively well studied case of ^{9}Li, and then applied to study the exotic, neutron unbound nucleus ^{13}Be. The isobaric analogue states are populated in proton resonant scattering with radioactive beams using the so called Thick Target Inverse Kinematics method [1]. The T=3/2 excited states in ^{9}Be (isobaric analogues of ^{9}Li) were populated with ^{8}Li + p scattering using the RESOLUT radioactive nuclear beam facility [2] at Florida State University. R-matrix calculations [3] were performed to describe the excitation function for the p+^{8}Li resonance elastic scattering using already known states in the T=3/2, A=9 isobaric system [4, 5]. This benchmark study demonstrated that the isobaric analogue (T=3/2) states indeed dominate the p+^{8}Li excitation function at low (with respect to the T=3/2, A=9 ground state) excitation energies and that reliable spectro-

scopic information, such as spin-parities and partial widths for these states, can be extracted. The new T=3/2, J^π=5/2$^+$ state in ^{9}Be at 18.5 MeV was observed for the first time, confirming the onset excitation energy of 4 MeV for the 2s$_{1/2}$ shell in the T=3/2, A=9 isobaric multiplet, which was recently observed for the first time in ^{9}C [5]. The results of this study are published in Ref. [6].

The Structure of the neutron unbound nucleus ^{13}Be was studied through T=5/2 isobaric analog states in ^{13}B, populated in proton resonant scattering on ^{12}Be. Previously structure of ^{13}Be has been extensively studied experimentally [7, 8, 9, 10, 11, 12, 13, 14] and theoretically [15, 16, 17, 18, 19, 20] but no consensus has been achieved on the structure of the ground state and other low-laying states of this exotic nucleus. The radioactive beam, ^{12}Be, for this experiment was produced by the TRIUMF ISAC II rare isotope beams facility. The excitation function for p+^{12}Be is shown to be dominated by T=5/2 resonances. The R-matrix analysis indicates that the experimental data can be described by two T=5/2 resonances in ^{13}B with spin-parities 1/2$^+$ and 5/2$^+$. These new data provide strong evidence that the ground state of ^{13}Be has spin-parity of J^π = 1/2$^+$, resolving the long-standing puzzle of the structure of ^{13}Be.

DEDICATION

To my parents and siblings, and my good friend Anna.

ACKNOWLEDGMENTS

I would first like to thank my adviser, Dr. Grigory Rogachev. I joined his research group in my first semester at Texas A&M and I can honestly say that without his support over my years here I never would have made it to the end. I also learned a great deal about being a scientist and mentorship from him that I will definitely take with me from here on out. I am truly fortunate to have joined his research group and consider joining one of the best decisions I've made in my life so far.

Next, I would like to thank the various members of my research group. Dr. Tony Ahn and Dr. Jack Bishop were very supportive in the time we've shared here and gave me constant assistance in my research. I have been very grateful for their presence. Dr. Yevgen Koshchiy was indispensible on experiments and for hardware assistance. Even when he couldn't physically be there for my experiment at TRIUMF his assistance was invaluable. Finally, while they were here as graduate students, Dr. Josh Hooker and Dr. Sriteja Upadhyayula were helpful in my research, on experiments, and navigating being a graduate student.

Special thanks to Dr. Charles Folden III, Dr. Jeremy Holt, and Dr. Dan Melconian for serving on my committee (and a special shout out to Dan, whom I had the pleasure of playing hockey with on several occasions).

Finally, I have to credit my friends I've met here in College Station with keeping me sane. Sean Wu, James Gerity, Derek Anderson, Tarini Konchady, Aaron Wood, Josh Winchell, Dawson Nodurft, Ryan Mueller, and many, many more that would take too long to write out. They were the best part of College Station and I will definitely miss every one. Additionally, a shout out to Rough Draught, where we spent many Friday nights together over the years.

CONTRIBUTORS AND FUNDING SOURCES

Contributors

This work was supported by a dissertation committee consisting of Professor Girgory V. Rogachev [advisor] and Professors Jeremy W. Holt and Dan G. Melconian of the Department of Physics and Astronomy and Professor Charles M. Folden III of the Department of Chemistry.

The data analyzed for Chapter III was acquired in an experiment performed at Florida State University by G.V. Rogachev, S. Almaraz-Calderon, A. Aprahamian, M. Avila, L.T. Baby, B. Bucher, V.Z. Goldberg, E.D. Johnson, K.W. Kemper, A.N. Kuchera, W.P. Tan, and I. Wiedenhöver.

The data analyzed for Chapter IV was acquired in an experiment performed at TRIUMF with assistance from G.V. Rogachev, E. Koshchiy, S. Ahn, J. Bishop, S. Upadhyayula, E. Aboud, A. Bosh, C. Parker, M. Roosa, B.T. Roeder from Texas A&M Cyclotron Institute, M. Alcorta from TRIUMF, and K. Hahn, and S. Han from Ewha Womans University, Seoul, South Korea.

All other work conducted for this dissertation was completed by the student independently.

Funding Sources

Graduate study was supported by a teaching assistantship from the Department of Physics and Astronomy and a research assistantship from the Cyclotron Institute. The dissertation research was funded from Office of Science, US Department of Department of Energy, grant # DE-FG03-93ER40773, and National Science Foundation under grant No. PHY-1712953 and No. PHY-1713857.

TABLE OF CONTENTS

Page

LIST OF FIGURES

LIST OF TABLES

TABLE Page

1. INTRODUCTION

1.1 Basic Nuclear Physics

1.1.1 Shell Model

In 1963, half of the Nobel Prize in Physics was awarded to Maria Goeppert Mayer and Johannes Hans D. Jensen for the development of the shell model of the nucleus. The nuclear shell model, as proposed by Goeppert Mayer over a decade earlier, described the experimentally observed nuclear structure surprisingly well. The protons and neutrons in a nucleus form closed shells at particular numbers of protons or neutrons. Goeppert Mayer was able to describe the experimental observation by using spin-orbit coupling, which split the levels of the square well potential to create shell gaps.

By the time the nuclear shell model was formulated in 1949, experimental evidence of shell closures had mounted. There was clear evidence of so called "magic numbers" of protons and neutrons for shell closures at 2, 8, 20, 28, 50 and 82. The Shell Model of the nucleus was developed to recover these magic numbers. This model treats the nucleus as individual nucleons with kinetic energy $T_i(r_i)$ moving in a potential field, $V(r)$ [21].

$$H = \sum_{i}^{A} T_i(r_i) + V(r) \tag{1.1}$$

The potential field covers the complex interaction between one nucleon and all the other nucleons in the nucleus. The simplest attempts at producing the structure of the nucleus would be to use either an infinite square well potential or the harmonic oscillator. Both methods reproduce the 2, 8, and 20 shell closures but not the rest. Additionally, a more realistic potential, the Woods-Saxon Potential, may be utilized.

$$V(r) = \frac{-V_0}{1 + \exp[(r - R)/a]} \tag{1.2}$$

The parameters of this intermediate potential are well defined by the number of nucleons and the binding energy with $R = r_0 A^{1/3}$, where r_0, the reduced radius, is typically around 1.25 fm, a is typically around 0.5 - 0.6 fm and V_0 is adjusted to get the correct separation energies but is generally on the order of 50 MeV. Unfortunately, even this, more realistic potential fails to reproduce the shell closures above 20.

As mentioned above, the major breakthrough was the addition of the spin-orbit interaction to the potential. In atomic physics, the spin-orbit interaction is electromagnetic in origin, however in nuclear physics it is the nucleon-nucleon interaction that gives rise to the spin-orbit term. The term is given by $V_{so}\mathbf{l} \cdot \mathbf{s}$. The term l, of course, is the orbital angular momentum of the level while s is the spin of the nucleon. As such we represent states using the total angular momentum, $\mathbf{j} = \mathbf{l} + \mathbf{s}$, where nucleons always have a spin with magnitude $s = 1/2$. Thus the spin-orbit term splits the level degeneracy into $j = l + 1/2$ and $j = l - 1/2$. With this splitting the correct magic numbers are recovered as seen in Figure 1.1.

1.1.2 Notation for nuclear states

When describing the total state of a nucleus, special notation is used: nuclear spin, notated with J or I, and parity, π. For nuclei that have an even number of protons and of neutrons, $J^\pi = 0^+$ for the ground state. For nuclei that have one set even and the other odd, $J = j$ of the unpaired nucleon for the ground state. For both protons and neutrons being odd the unpaired nucleons can couple to any integer value from $J = |j_p - j_n|$ to $J = j_p + j_n$. For example, in the cases of ^{2}H, ^{6}Li, and ^{14}N the ground state spin is 1 and ^{10}B has a ground state spin of 3.

The parity operator produces a mirror reflection image, as such the measure of parity is directly related to l. The wavefunction for even l is symmetric, thus parity for even l is $\pi = +1$, while for odd l the wavefunction is anti-symmetric leading to $\pi = -1$. In this way, for a single nucleon its parity is $\pi = (-1)^l$. The parity of a whole nucleus is the product of the parity of all nucleons that comprise it. Since paired nucleons will always produce a product of 1 we once again only need to consider unpaired nucleons. For an example, ^{9}Be has 4 protons and 5 neutrons; the only unpaired nucleon is the spare neutron. The spare neutron is in the $p_{3/2}$ level in the ground state so it has $J^\pi = 3/2^-$.

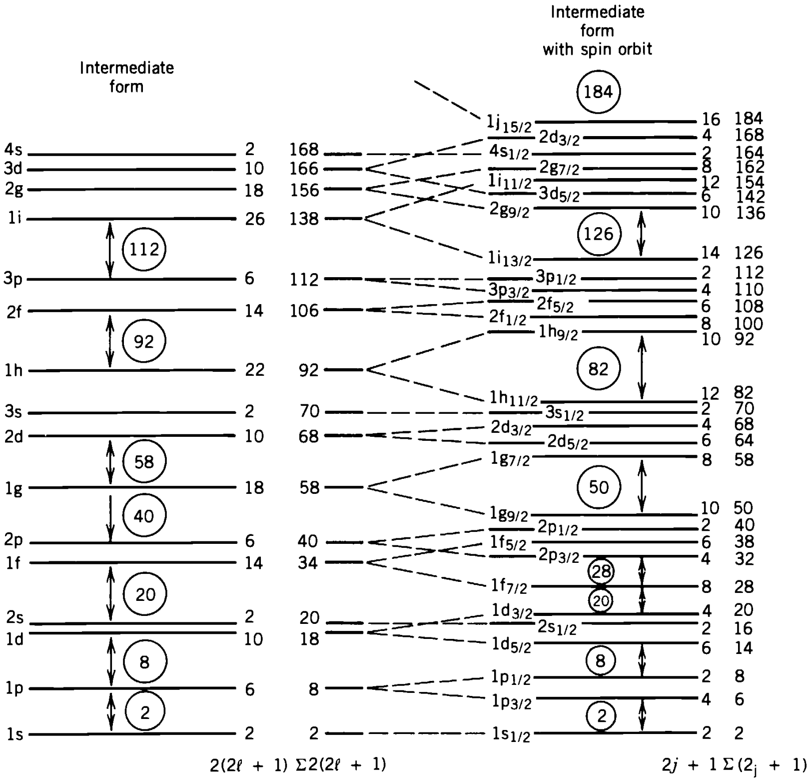

Figure 1.1: The shell model, along with the magic numbers derived as a consequence of potentials used. The left shows the results with the Woods-Saxon potential while the right shows the results with the Woods-Saxon potential and the additional spin-orbit term. Reprinted with permission from [21]

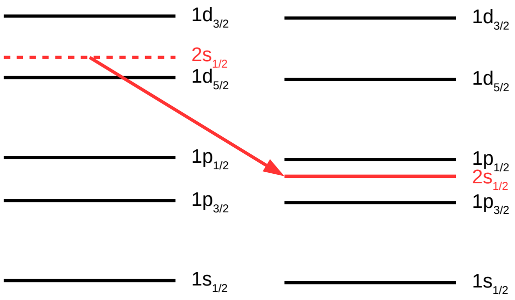

Figure 1.2: A level scheme showing the $2s_{1/2}$ state dropping out of the 2s1d shell into the 1p shell as seen in beryllium isotopes, most famously ^{11}Be.

1.2 Shell Evolution

1.2.1 Intruder States and Inversion

The Shell Model, in its basic form, works well for stable nuclei, but it has been observed to describe poorly some exotic nuclei. By 1960, it was recognized that ^{11}Be had a ground state spin-parity of $1/2^+$ [24]. The ^{11}Be nucleus has 4 protons and 7 neutrons, therefore the shell model predicts the 7th neutron to be in the $1p_{1/2}$ level which would give $J^\pi = 1/2^-$. The explanation of this discrepancy is that the $2s_{1/2}$ level in ^{11}Be is actually at a lower energy than the $1p_{1/2}$ level and is thus filled first [24]. This $2s_{1/2}$ level is an example of an "Intruder State" as shown in Figure 1.2. This inversion is also witnessed in excited states of ^{9}Be and ^{10}Be [24].

This inversion gets more interesting in the case of ^{12}Be where the ground state is actually a mix of ^{10}Be$\otimes(2s_{1/2})^2$, ^{10}Be$\otimes(1p_{1/2})^2$ and ^{10}Be$\otimes(1d_{5/2})^2$ [25]. While unbound, ^{13}Be continues the trend of unusual behavior in neutron-rich beryllium isotopes with a general disagreement on whether the inversion exists in its ground state or not. The topic of the ^{13}Be ground state is studied in more detail in this thesis.

1.2.2 Shell Closures and Magic Numbers

Another significant result of shell evolution is the disappearance of shell closures that exist for stable nuclei as predicted by the shell model. The oxygen isotopes are a classic example of shell evolution. At present oxygen is the heaviest element where the entire nucleon bound isotopic chain has been studied. Experiments on ^{22}O and ^{24}O, the heaviest bound oxygen isotopes, showed that the shifting of states leads to closed shells at $N = 14$ and $N = 16$, respectively, for these isotopes. This evolution in shell closures, and thus the magic numbers, has important consequences for the structure of the Oxygen isotopic chain and is responsible for ^{24}O being the last bound Oxygen isotope.

1.3 Ab Initio Models

The study of shell evolution is important to the development of theoretical models of nuclear structure and the nucleon-nucleon interaction. In the treatment of the Shell Model above, a central potential and a spin orbit potential were used to describe the interaction of a nucleon with the rest of the nucleus. *Ab initio* models seek to do better than this by using the actual interactions between the individual nucleons. We have a nucleus with A nucleons where each pair ij of nucleons interact with the nucleon-nucleon interaction which is repulsive at short distances and attractive at medium distances. This interaction, $V^{(2)}(\mathbf{r}_i - \mathbf{r}_j)$, is discussed in more detail below. In addition to the nucleon-nucleon interaction three body forces between ijk nucleons are also often used, $V^{(3)}(\mathbf{r}_i - \mathbf{r}_j, \mathbf{r}_i - \mathbf{r}_k)$.

The main goal would be to exactly solve for the nuclear wave function, $\Phi(\rho_1, ..., \rho_{A-1})$, where $\rho_i = \mathbf{r}_i - \mathbf{S}$ is the position of the nucleon relative to the center of mass of the nucleus. We are interested in the eigensolution, $\Phi_{I\mu}$, for a total nuclear spin, I, and z-projection, μ. The Schrödinger equation then is:

$$H_A \Phi_{I\mu}(\rho_1, ..., \rho_{A-1}) = E_I \Phi_{I\mu}, \tag{1.3}$$

where E_I is the energy eigenvalue of the solution. The Hamiltionian, H_A is the sum of the kinetic and potential energies of the particles not counting the motion of the center of mass of the system. One way of writing the kinetic part is to add up the kinetic energy of the particles with mass m_i and position r_i then subtract the kinetic energy of the motion of the center of mass with mass M and position S.

$$H_A = -\sum_{i=1}^{A} \frac{\hbar^2}{2m_i}\nabla^2_{\mathbf{r}_i} + \frac{\hbar^2}{2M}\nabla^2_{\mathbf{S}} + \sum_{i>j}^{A} V^{(2)}(\mathbf{r}_i - \mathbf{r}_j) + \sum_{i>j>k}^{A} V^{(3)}(\mathbf{r}_i - \mathbf{r}_j, \mathbf{r}_i - \mathbf{r}_k) \tag{1.4}$$

While an easy problem to set up, solving $(H_A - E_I)\Phi_{I\mu}$ is challenging. The nucleon-nucleon interactions and three body forces are not explicitly known, however realistic calculations of these potentials have been performed and experimental constraints can be imposed as discussed below. The computational power required to solve the equations numerically becomes the greatest challenge. Most *ab initio* methods use some form of approximation to simplify the problem to make it solvable. Several *ab initio* methods exist for performing the calculation and two prominent ones, Green's Function Monte Carlo (GFMC) and No Core Shell Model (NCSM) are discussed below.

1.3.1 Nucleon-Nucleon Interaction

The nucleon-nucleon interaction mentioned above is not explicitly known, however there is much that is known about it from observations of nucleons and nuclei. To start, the nuclear interaction is attractive on the order of the nuclear radius and is much stronger than the Coulomb interaction. It is also repulsive at the nucleon radius to prevent nucleons from occupying the same space. Another important property of the nucleon-nucleon interaction is that it is charge independent and isospin invariant. Deuterons only have a single bound state, the 1^+ ground state, even though its two nucleons could have the spins be either aligned or anti-aligned. The spin and parity of 1^+ indicates the spins are aligned and the orbital angular momentum of the nucleons is 0 or 2. With the spins aligned the nucleons are bound, but when they anti-align they are no longer bound as there is no bound 0^+ state. This indicates that the interaction between nucleons is spin dependent.

For *ab initio* calculations a better defined nucleon-nucleon interaction is needed. The nucleon-nucleon interaction at a fundamental level is just the residual strong force interaction that binds quarks together to form protons and neutrons. The theory of the strong force interaction, Quantum Chromodynamics (QCD), is the field theory that describes the interaction between quarks and gluons. To bring things up to the nucleon scale an effective field theory based on the symmetries of QCD is constructed, called Chiral Effective Field Theory (χEFT). The nucleon-nucleon (NN) and three-nucleon (NNN) interactions are obtained from calculating higher order terms in the expansion of the potential.

1.3.2 No Core Shell Model

Shell Model calculations typically utilize an inert core to reduce the model space, therefore reducing the calculation time. However No Core Shell Model (NCSM) [26] calculations include every nucleon in the calculation, made possible by advances in computational power. To solve Equation 1.4 for all nucleons using realistic nucleon-nucleon and three nucleon interactions, such as those from χEFT, a Harmonic Oscillator basis is used. This basis is truncated at a maximum total energy, N_{max}, of the A-nucleon system to make the calculation feasible by reducing the model space to $N_{max}\hbar\Omega$ harmonic oscillator states. With a sufficiently large basis size the calculation will typically converge. NCSM calculations with χEFT interactions have been effective at calculating low A systems where a significant amount of experimental data is already available, such as A=7, A=8, and A=10, due to the smaller basis size [26]. NCSM runs into computational limitations for heavier nuclei, though has been applied up to ^{20}C [26]. The NCSM method is still ongoing development and will require more experimental data on neutron rich nuclei.

1.3.3 Green's Function Monte Carlo

While NCSM has been quite successful for *ab initio* calculations, it is not the only method employed. Quantum Monte Carlo (QMC) methods have been utilized to calculate many properties of nuclei, including low energy nuclear spectra and transitions for light nuclei [27]. A few methods exist that employ QMC methods, but they generally start with the Variational Monte Carlo (VMC) method. In VMC, a trial wave function, Ψ_T, is assumed and variational parameters are optimized by minimizing the energy. The energy, E_V, of the trial wavefunction is always greater than or equal to the ground-state energy, E_0.

$$E_V = \frac{\langle\Psi_T|H|\Psi_T\rangle}{\langle\Psi_T|\Psi_T\rangle} \geq E_0 \tag{1.5}$$

Greens Function Monte Carlo (GFMC) begins with a minimized trial wave function from VMC and projects the wave function along imaginary time, τ, using Monte Carlo methods.

$$|\Psi_0\rangle \propto \lim_{\tau\to\infty} exp[-(H - E_0)\tau]|\Psi_T\rangle \tag{1.6}$$

1.4 Reaction Studies

1.4.1 Nuclear Reactions

Ab initio calculations are very effective at calculating the properties of nuclear systems that have already been studied, however this is often done with less constrained 3-body forces. Testing the predictive power of these models for less studied exotic nuclei is important. The structure of exotic nuclei can be studied through a variety of methods, one of which is studying the interaction between two particles. In these reactions a beam particle, or projectile (A), interacts with a stationary target particle (B) and from there a number of outcomes is possible, the most basic of which is the binary reaction, $B(A, D)C$.

$$A + B \rightarrow C + D \tag{1.7}$$

The structure of a nucleus involved in a reaction can be determined from the cross section of the reaction using various methods such as R-Matrix and Distorted Wave Born Approximation (DWBA), the former of which is explained in detail in the next chapter.

The simplest binary reaction is *elastic scattering*, $B(A, A)B$, where the particles exiting the reaction are in the same state as they went in. In contrast to elastic scattering there is *inelastic* *scattering*, $B(A,A)B^*$ for instance, where some of the energy of the system is used to raise one of the particles, B here, to an excited state instead of leaving it in the ground state.

Sometimes when the particles are interacting, a nucleon (proton or neutron) or a group of nucleons may be exchanged where nucleons are removed from one nucleus and transferred to the other. These kinds of reactions are, appropriately, named *transfer reactions*. In transfer reactions some of the nuclei can be treated as a core plus the transferred nucleons, such as neutron transfer in $(A = D + n) + B \rightarrow (C = B + n) + D$.

In *capture* reactions, the interacting particles form a composite in an excited state that can live long enough to decay to the ground state either by having the excess energy taken away by another particle or to decay by γ emission, denoted by $B(A,\gamma)D$. *Knockout* or *breakup* reactions are a case where one of the interacting particles breaks up into one or more particles, $B(A, C + D)B$.

1.4.2 Direct Reactions

Direct reactions are reactions where predominantly the surface nucleons interact. These interactions will be on a very short time scale, on the order of 10^{-22} s and will typically only involve a few valence nucleons. Cross section calculations for direct reactions are often performed with DWBA methods. Calculations done this way are performed using structure information, which can be determined by comparing the calculation with the experimentally determined cross sections.

1.4.3 Compound Nucleus Reactions

A contrast to direct reactions are compound nucleus reactions. In compound nucleus reactions an incident nucleon or particle will interact with the entire nucleus, spreading its energy throughout and temporarily forming a compound nucleus in an excited state (X^*) where all involved nucleons are interacting. This compound nucleus will be relatively long lived, on the order of 10^{-16} to 10^{-21}s. Eventually, excited state X^* decays, for example:

$$A + B \rightarrow X^* \rightarrow C + D \tag{1.8}$$

In compound nucleus reactions all information about the initial particles is lost as the compound nucleus is formed [28]. This loss of information means that the relative probability for each outgoing channel is independent of the initial reaction.

1.4.4 Resonance Reactions

Nucleons involved in a reaction can become temporarily trapped by a potential barrier. These nucleons will still be unbound but the state can be relatively long lived at low energies. These unbound states are called resonances. At higher excitation energies, the lifetimes of resonances will become shorter, widths becoming larger, leading to a structureless continuum. Resonances can be described by the R-matrix formalism [3]. The R-matrix, a method detailed in the next chapter and used in the structure studies in this thesis, is most effective when the number of resonances is limited as the calculations become very unwieldy as more resonances are included. The statistical Hauser-Feshbach model [29] can be applied to evaluate the cross section for a compound nucleus reaction in the energy region where individual resonances cannot be resolved.

Resonances can form for many reasons. A potential barrier, such as the Coulomb barrier for protons, can temporarily trap protons at low energies. These trapped protons are not fully bound, but form resonances that survive for a finite time. Another barrier is the centrifugal barrier, which exists for all nucleons when $L > 0$, which can also allow nucleons to form resonances. Yet another consideration is structural limitations on particle decay. An example is isospin conservation for low laying $T = 3/2$ states in ^{9}Be (a system studied in this thesis). The two lowest energy $T = 3/2$ states in ^{9}Be are below the proton decay threshold and the lowest three $T = 3/2$ states are below the threshold for neutron decay to isospin allowed $T = 1$ states in ^{8}Be. Because of this, the lowest two $T = 3/2$ states are fairly narrow resonances, on the order of hundreds of eV. It is possible for nearly-bound, $L = 0$, single particle neutron states to form a virtual state which manifest in a rapid rise of the cross section toward zero energy and can be described by a large, negative scattering length.

1.5 Conclusion

The study of the structure of exotic nuclei is of interest due to the shell evolution exhibited by nuclei far from stability. Experimental study of shell evolution informs our understanding of the nucleon-nucleon interaction and provides a benchmark for further development of *ab initio* methods. In this thesis, I present a method for studying the structure of neutron rich nuclei through their isobaric analogue states using resonant scattering. This method was explored in the study of high isospin states in ^{9}Be. The method was then applied to the study of the ground and low-laying states of ^{13}Be through its isobaric analogue states in ^{13}B. The results of both studies are presented in this thesis.

2. RESONANT SCATTERING WITH ISOBARIC ANALOGUE STATES

2.1 Introduction

Neutrons and protons have roughly the same mass and while their charge is different, the Coulomb interaction is quite small compared to the force between nucleons. The nuclear force is charge independent and symmetric with respect to interchange between protons and neutrons. It is useful to introduce an isospin symmetry by representing protons and neutrons as two isospin states of the same particle (nucleon), with the neutron defined by $t_z = 1/2$ and the proton defined as $t_z = -1/2$, though the sign choice is arbitrary. For the isospin of a composite system of two or more nucleons, the isospins are coupled to a total isospin

$$\hat{\mathbf{T}} = \sum_{k} \hat{\mathbf{t}}_{\mathbf{k}} \tag{2.1}$$

The z-component can be defined as $T_z = \frac{1}{2}(N - Z)$ where N and Z are the number of neutrons and protons, respectively. In nuclei with the same number of nucleons, levels with the same internal structure (isospin, spin, and parity) will exist and will have the same energy, perturbed slightly by the Coulomb interaction. These states are called isobaric analogue states.

The experiments performed and analyzed in this thesis used resonant scattering to study the structure of isobaric analogue states in exotic nuclei. Resonance elastic scattering performed in inverse kinematics with radioactive ion beams is an effective way of populating resonances in exotic nuclei. R-Matrix calculations can be employed to reproduce the excitation function of resonant scattering and obtain observable information about the energy, width, spin, and parity of the resonances.

Resonant scattering utilizing the Thick Target in Inverse Kinematics (TTIK) method and analyzed with the R-Matrix, as described in this chapter, has been a powerful tool in the study of exotic nuclei [30][5]. Applying these same methods to the study of neutron-rich nuclei, however, is complicated by the need for a neutron target. Studying the proton-rich mirror nuclei is not always possible as the mirror of nuclei near the neutron dripline are often unbound. It was suggested by V. Goldberg [31] that isobaric analogue states could be studied with resonant scattering to infer information about the structure of neutron-rich nuclei.

2.2 Resonant Scattering

2.2.1 Reaction Kinematics for Elastic Scattering

Resonant scattering experiments study the scattering of two nuclei, populating resonances in the compound nucleus. The excitation function (cross section as a function of energy) for resonant elastic scattering provides valuable information about the structure of the resonances in the compound nucleus. Experiments are performed with a stationary target, A, interacting with a projectile, B, from an accelerator. This simplifies the kinematics so the energy and momentum conservation of the initial and final states are as follows.

$$E = \frac{1}{2}m_B v_{Bi}^2 = \frac{1}{2}m_A v_{Af}^2 + \frac{1}{2}m_B v_{Bf}^2 \tag{2.2}$$

$$\mathbf{p} = m_B \mathbf{v_{Bi}} = m_A \mathbf{v_{Af}} + m_B \mathbf{v_{Bf}} \tag{2.3}$$

The scattering angle of the outgoing particles can be related through the following.

$$\sin(\theta_B) = \sqrt{\frac{m_A E_{Af}}{m_B E_{Bf}}} \sin(\theta_A) \tag{2.4}$$

It is useful to look at the center of mass frame instead of the laboratory frame. The transformation from lab to center of mass energy is

$$E_{cm} = \frac{m_A}{m_A + m_B} E_{lab} \tag{2.5}$$

In this frame of reference, the relation between the energy of the particles is easy to calculate

$$E_A = \frac{m_B}{m_A + mB} E_{cm} \tag{2.6}$$

$$E_B = \frac{m_A}{m_A + mB} E_{cm} \tag{2.7}$$

The center of mass angle is given by

$$\theta_{cm} = \pi - 2\theta_A \tag{2.8}$$

The reduced mass of the system is given by

$$\mu = \frac{m_a m_b}{m_a + m_b} \tag{2.9}$$

In addition to elastic scattering other types of reactions can occur in resonant scattering studies. Inelastic scattering can occur, where the compound nucleus decays into an excited state of one of the outgoing nuclei, as well as where the outgoing particles are different from the incoming ones. In the latter case the difference between the rest energy of the initial and final particles, the Q-value, must be accounted for in energy conservation.

2.2.2 Cross Section

The cross section, (σ), measured as a function of energy - the excitation function - can be used to determine information about the structure of nuclei. The cross section is related to the ratio of the outgoing particles to incoming particles and thus is a measure of the probability of the reaction occuring. Cross section is measured in cm^2, though it is generally reported in units of barns, 1 barn $=$ 10^{-24} cm^2. Differential cross section, $d\sigma/d\Omega$, is a measure of the cross section dependence on scattering angle. Measured experimentally, the efficiency corrected differential cross section is found with the following

$$\frac{d\sigma}{d\Omega} = \frac{N}{N_{in}} \frac{1}{T_t \Omega} \tag{2.10}$$

Where N is the particles measured in the detector, N_{in} is the total number of incoming particles (beam ions), T_t is the number of target particles per unit area for the given energy bin, and Ω is the solid angle of the detector seen from the target position.

Finding the differential cross section in the center of mass frame is useful. Converting from the laboratory frame to center of mass frame differential cross section involves converting the solid angle from the lab frame to center of mass frame and is given by

$$\frac{d\sigma}{d\Omega}_{cm} = \frac{d\cos\theta_{lab}}{d\cos\theta_{cm}}\frac{d\sigma}{d\Omega}_{lab}. \tag{2.11}$$

For the elastic scattering kinematics for recoil A, the c.m. and lab frame scattering angles are related as in Equation 2.8 and therefore becomes:

$$\frac{d\sigma}{d\Omega}_{cm} = \frac{1}{4\sin\left(\frac{\theta_{cm}}{2}\right)}\frac{d\sigma}{d\Omega}_{lab} \tag{2.12}$$

2.2.3 Thick-Target Inverse Kinematics

Performing resonant scattering in regular kinematics involves using a lighter particle, such as a proton or an α-particle, as a projectile and a heavier particle as a target. Inverse kinematics, on the other hand, uses the heavier particle as a projectile and the lighter particle as the target. An advantage to inverse kinematics is that it allows the use of radioactive ion beams in resonant scattering to explore the structure of exotic nuclei. Another advantage is improved center of mass energy resolution as the lab energy will be several times larger than the center of mass energy in inverse kinematics, but they will be nearly equal in direct kinematics.

The use of inverse kinematics with a thick target, an even more powerful method, was first introduced in [32]. In this method, called Thick Target Inverse Kinematics (TTIK) [1], the beam projectiles lose energy as they pass through the target allowing for measurements at a range of lab energies for a single beam energy. To measure a range of energies with a thin target, the energy of the beam from the accelerator must be varied, costing time as the accelerator is retuned. Another advantage is the entire range of energies can be measured simultaneously, yielding higher statistics for the same run time. This increase in efficiency is important when using radioactive ion beams, produced as secondary beams, as the number of beam particles per second is typically orders of magnitude lower compared to stable primary beams.

2.3 R-Matrix

2.3.1 Introduction

The R-Matrix theory was first introduced in 1947 by Wigner and Eisenbud [33]. Lane and Thomas [3], in 1958, developed the use of R-Matrix for describing nuclear resonances. R-Matrix theory divides the configuration space into internal and external regions with the boundary defined by a parameter called the channel radius, a. The R-Matrix used for calculating resonances is called the phenomenological R-Matrix [34][35] and parametrizes various physical processes for the calculation of cross sections. The R-Matrix can also be applied as a way of solving the Schrödinger equation, particularly in coupled-channel problems with many open channels, called the calculable R-Matrix. For the work in this thesis the phenomenological R-Matrix was a significant tool for understanding resonant scattering spectra.

2.3.2 Scattering

Solving the Schrödinger equation for scattering in a central potential is used as a starting place. At large r the potential is merely the Coulomb potential.

$$V(r) \rightarrow_{r\rightarrow\infty} V_C(r) = \frac{Z_1 Z_2 e^2}{4\pi\epsilon_0 r} \tag{2.13}$$

The potential at smaller r would be the Coulomb potential plus an additional term. For a central potential in spherical coordinates, the radial and angular wavefunctions can be factored apart as follows:

$$\psi(r,\theta,\phi) = \frac{1}{r} u_l(r) Y_l^m(\theta,\phi) \tag{2.14}$$

Here the function $u_l(r)$ is some radial wavefunction. The radial Schrödinger equation for partial wave l for the wavefunction $u_l(r)$ is

$$(\hat{H}_l - E)u_l = 0. \tag{2.15}$$

With $\hat{H}_l$ as the radial Hamiltonian

$$\hat{H}_l = \hat{T}_l + V(r) \tag{2.16}$$

$$\hat{T}_l = -\frac{\hbar^2}{2\mu_c}\left(\frac{\mathrm{d}^2}{\mathrm{d}r^2} - \frac{l_c(l_c+1)}{r^2}\right) \tag{2.17}$$

The wavefunction, $u_l(r)$ must become zero at the origin since $\psi(r, \theta, \phi)$ must be finite at the origin.

$$u_l(0) = 0 \tag{2.18}$$

Asymptotically, the wavefunction can be written in terms of the regular and irregular Coulomb functions, F_l and G_l.

$$u_l(r) \to \cos\delta_l F_l(\eta, kr) + \sin\delta_l G_l(\eta, kr) \tag{2.19}$$

Here δ_l is the phase shift and η is the Sommerfeld parameter defined as

$$\eta = \frac{Z_1 Z_2 e^2 \mu}{4\pi\epsilon_0\hbar^2 k}. \tag{2.20}$$

Alternatively Equation 2.19 can be written as

$$u_l(r) \to \frac{i}{2}\left[I_l(\eta, kr) - U_l O_{l(\eta,kr)}\right], \tag{2.21}$$

where $I_l = G_l - iF_l$ and $O_l = G_l + iF_l$ and U_l is the scattering matrix, often called the S-Matrix, defined as

$$U_l = e^{2i\delta_l} \tag{2.22}$$

The total differential cross section can be written as a combination of the solutions for the Coulomb scattering and for the extra part of the potential.

$$\frac{\mathrm{d}\sigma}{\mathrm{d}\Omega} = |f_C(\Omega) + f(\Omega)|^2 \tag{2.23}$$

where $f_C(\Omega)$ is the Coulomb scattering amplitude

$$f_C(\Omega) = -\frac{\eta}{2k\sin^2\frac{1}{2}\theta}\mathrm{e}^{2\mathrm{i}(\sigma_0 - \eta \ln \sin\frac{1}{2}\theta)} \tag{2.24}$$

and $f(\Omega)$ is the additional scattering amplitude

$$f(\Omega) = \frac{1}{2ik}\sum_{l=0}^{\infty}(2l+1)e^{2i\sigma_l}(U_l - 1)P_l(\cos\theta) \tag{2.25}$$

In the scattering amplitudes above, σ is the Coulomb phase shift and k is the wave number.

2.3.3 R-Matrix

As mentioned above the R-Matrix theory separates the external and internal regions. The external wavefunction can be approximated as the asymptotic behaviour.

$$u_l^{ext} = \frac{i}{2}\left[I_l(\eta, kr) - U_l O_{l(\eta,kr)}\right] \tag{2.26}$$

At the interface between the internal and external wavefunctions, the channel radius $r = a$, the wavefunction can be written in terms of the R-Matrix.

$$u_l(a) = R_l(E)[au_l^{'}(a) - Bu_l(a)] \tag{2.27}$$

Here B is an arbitrary boundary parameter and $u_l^{'}(a)$ is the value of the radial derivative of $u_l(r)$ at $r = a$. A convenient selection for this boundary parameter will be introduced later. By combining this definition with Equation 2.26 the collision matrix can be defined by the R-matrix.

$$U_l = \mathrm{e}^{2i\phi_l}\frac{1-(L_l^*-B)\,R_l}{1-(L_l-B)\,R_l} \tag{2.28}$$

where

$$L_l = ka\frac{O_l^{'}}{O_l}, \tag{2.29}$$

with $O_l^{'}$ being the radial derivative of O_l, and

$$\phi_l = \arg I_l(ka) = -\arctan[F_l(ka)/G_l(ka)] \tag{2.30}$$

where ϕ_l is the hard-sphere phase shift. The single channel R-matrix, such as in elastic scattering, for N states is

$$R_l(E) = \sum_{n=1}^{N}\frac{\gamma_n^2}{E_n-E} \tag{2.31}$$

There are a few important quantities in this definition of the R-Matrix. The reduced width amplitude, γ_n, is related to the observable width, Γ, of the resonance but is not itself an observable as it depends on choice of channel radius and boundary condition. Likewise the energy eigenvalue of the resonance, E_n, is not an observable but can be used to calculate the observable energy of the resonance.

For multiple channels, c and c'

$$R_{cc'}(E) = \sum_{n=1}^{N}\frac{\gamma_{nc}\gamma_{nc'}}{E_n-E} \tag{2.32}$$

The differential cross section can, therefore, be calculated from the R-Matrix. In principal, the R-Matrix needs to be defined for all resonances in the compound nucleus and all possible exit channels. In practice, only the most relevant resonances and channels for the energy range measured are required.

As stated above the parameters for the R-Matrix are not observables. These parameters depend on the choice of channel radius and boundary condition. The observable resonance energy and width can be calculated from the energy eigenvalue and the reduced width amplitudes. To begin, the quantity L_l can be rewritten in terms of a penetrability factor, P_l, and a shift factor S_l.

$$L_l = S_l + iP_l \tag{2.33}$$

$$P_l(E) = \frac{ka}{F_l(ka)^2 + G_l(ka^2)} \tag{2.34}$$

$$S_l(E) = P_l(E)[F_l(ka)F_l^{'}(ka) + G_l(ka)G_l^{'}(ka)] \tag{2.35}$$

With the penetrability factor and the shift factor the observable energy and observable width for a resonance can be calculated from the energy eigenvalue and the reduced width amplitudes. Starting with the observable width, Γ_R, an observable reduced width amplitude, γ_{Rc}, is defined

$$\gamma_{Rc}^2 = \frac{\gamma_c^2}{1 + \gamma_c^2 S_l^{\prime}(E_n)} \tag{2.36}$$

The function $S_l^{\prime}(E)$ is the derivative of $S_l(E)$ with respect to energy. From here the observable energy for the resonance, E_R can be calculated

$$E_R = E_n - \sum_c \left[S_c(E_n) - B\right] \gamma_{Rc}^2 \tag{2.37}$$

S_c is the shift function for channel c. If the quantity in brackets is 0 then the energy eigenvalue will be equal to the observable resonance energy. This makes it convenient to choose a boundary condition that is equal to the shift function. One must be careful as the choice of boundary condition can only be made once for each J^{π}. For the observable partial width, Γ_{Rc},

$$\Gamma_{Rc} = 2\gamma_{Rc}^2 P_l(E) \tag{2.38}$$

The total width of the resonance, Γ_R, is therefore:

$$\Gamma_R = \sum_c \Gamma_{Rc} \tag{2.39}$$

The observable reduced width can be related to the single particle width through

$$\gamma_{Rc}^2 = SC^2\gamma_{sp}^2 \tag{2.40}$$

where S is the spectroscopic factor and C is the isospin Clebsch-Gordan coefficient for the channel. The single particle width, γ_{sp}, is related to the Wigner limit,

$$\gamma_w^2 = \frac{\hbar^2}{\mu a^2}, \tag{2.41}$$

or it can be calculated using a realistic potential, such as Woods-Saxon.

2.3.4 R-Matrix with Isobaric Analogue States

When studying the isobaric analogue states of neutron rich nuclei, these states will generally be highly-excited states in the continuum, where the width of states may be much greater than the average separation between states. The higher isospin states of interest, however, may be relatively narrow due to a limited number of open decay channels as a result of isospin conservation. Generally the lower isospin states will be broad, forming a background. One way of modeling this background is to perform optical model calculations and directly use the optical model phase shift in the R-matrix calculations, as suggested by D. Robson [36]. Alternatively, one can parameterize the broad continuum states using so called "background" resonances, which are usually introduced at much higher energy than the region of interest and produce a smooth variation of the phase shift as a function of energy. I used the second approach in the R-Matrix analysis presented in this thesis. R-Matrix calculations can thus be performed for the narrow high isospin states of interest without explicitly including the broad low isospin states.

3. BENCHMARKING RESONANT SCATTERING WITH ISOBARIC ANALOGUE STATES THROUGH THE A=9, T=3/2 ISOBARIC QUARTET [*]

3.1 Introduction

To benchmark the application of resonant scattering with isobaric analogue states ^{9}Be was chosen as a test case. ^{9}Be makes an interesting nucleus to study since the first three states in the A=9, T=3/2 isobaric quartet have been, to some degree, studied already in ^{9}Li, ^{9}Be, and ^{9}C, with the second excited state appearing above the proton threshold in ^{9}Be [37]. Additionally the sd-shell of the A=9, T=3/2 quartet was expected to be near the energy region of interest. The onset energy of this shell has recently been identified in ^{9}C [5]. The goal was to perform ^{8}Li(p,p) scattering to populate the isospin 3/2 states. Knowledge of the system from previous studies on ^{9}Li, ^{9}Be, and ^{9}C can be used to inform the parameters of the R-matrix calculation making the study of ^{9}Be a good test case of resonant scattering study of isobaric analogue states.

3.2 A=9, T=3/2 Isobaric Quartet

The most recent compilation on the A=9, T=3/2 isobaric quartet was in 2004 [37]. Since then, studies on ^{9}Li [4, 38, 39] and ^{9}C [30, 40, 5] have shed additional light on the system. The ground state of the quartet is a $3/2^{-}$ state, followed by a $1/2^{-}$ state and a $5/2^{-}$ state. A $5/2^{+}$ state was recently observed in ^{9}C in the vicinity of the $5/2^{-}$ state [5]. The level scheme of the quartet is shown in Figure 3.1. Of particular interest to any R-Matrix analysis involving these states are the spin, parity, width, and spectroscopic factors (where available).

3.2.1 ^{9}Be

The T=3/2 states in ^{9}Be have not been extensively studied above the proton threshold at 16.89 MeV. The first three T=3/2 states in ^{9}Be have been reported at 14.4 MeV, 16.98 MeV and 18.65

---

[*] Partially reprinted with permission from "Observation of $T = 3/2$ isobaric analog states in $^{9}\mathrm{Be}$ using $p +^{8}$ Li resonance scattering" by Hunt, C. and Rogachev, G. V. and Almaraz-Calderon, S. and Aprahamian, A. and Avila, M. and Baby, L. T. and Bucher, B. and Goldberg, V. Z. and Johnson, E. D. and Kemper, K. W. and Kuchera, A. N. and Tan, W. P. and Wiedenhöver, I., 2020, *Phys. Rev. C*, vol. 102, p. 014615, Copyright 2020 by American Physical Society.

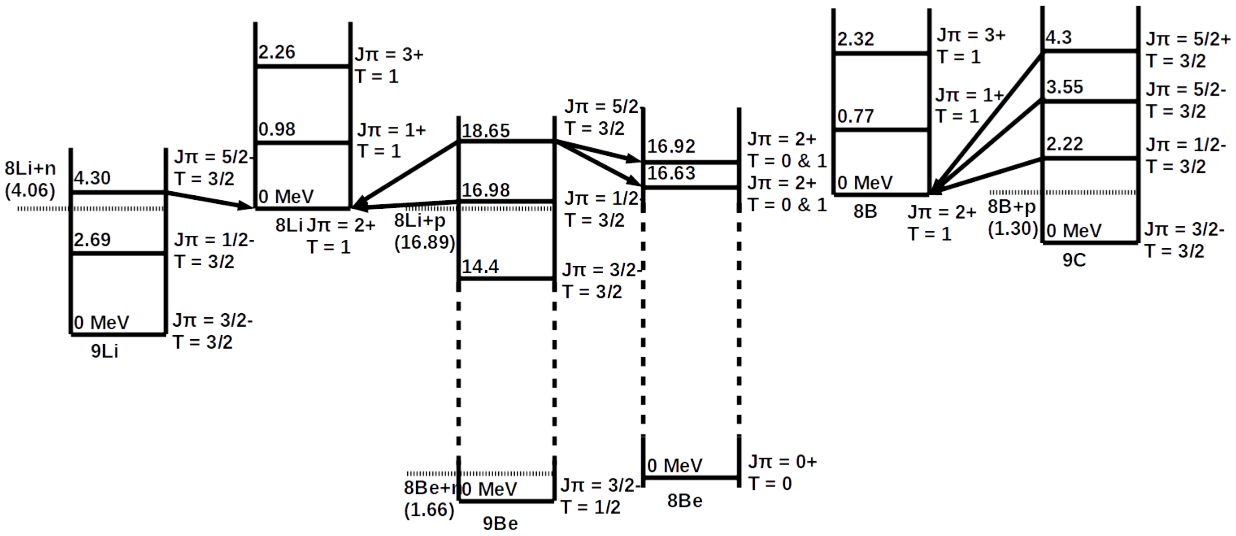

Figure 3.1: A partial level structure and decay channels of ^{9}Li, ^{9}Be and ^{9}C.

MeV [37]. The first two states have been well studied establishing the energy, spin, parity and isospin of these states. Much less is known about the 18.65 MeV state. Through the study of the decay of $^{9}_{\Lambda}$Li (a lithium nucleus where one of the neutrons in substituted with a Lambda baryon that decays to a proton) in 1985, the state was established as a T=3/2 state with a width of 300 keV [41]. The spin and parity were not assigned as the study was not sufficiently sensitive to the spin and parity to make a determination, though the state was associated with the analogous state in ^{9}Li which is now known to be $5/2^{-}$.

3.2.2 ^{9}Li

There are several states in ^{9}Li that have been observed: a $3/2^{-}$ ground state, a $1/2^{-}$ excited state at 2.69 MeV, a $5/2^{-}$ excited state at 4.31 MeV, and additional states at 5.38 MeV and 6.71 MeV [37][4]. The most recent studies of ^{9}Li have all been with transfer reactions analyzed with Distorted Wave Born Approximation (DWBA), ^{2}H(^{8}Li, p) [4][39] and ^{2}H(^{9}Li, t) [38]. The width of the $5/2^{-}$ state of interest in ^{9}Li is 100 keV [4].

3.2.3 ^{9}C

Recent studies on ^{9}C have been performed with elastic and inelastic scattering, greatly expanding our knowledge of ^{9}C and the A=9, T=3/2 isobaric quartet. Inelastic scattering of ^{9}C off a ^{9}Be target was used to determine the energies and widths of the first four excited states in ^{9}C using the invariant mass technique [40]. The second excited state was observed at 3.6 MeV, while the third excited state was observed at an energy of 4.4 MeV and given a tentative spin-parity of $1/2^{+}$ or $5/2^{+}$. Meanwhile, ^{8}B+p elastic scattering was utilized to give the second excited state a spin-parity assignment of $5/2^{-}$[30]. With a larger energy and angular range via a backgroundless measurement made possible by the active target approach, a firm $5/2^{+}$ assignment has been given for the 4.3 MeV state [5]. The states of interest, the $5/2^{-}$ and $5/2^{+}$, have widths of 1.1 MeV and 4.0 MeV respectively.

3.3 Experiment

An experiment was carried out at the RESOLUT radioactive nuclear beam facility [2] at the John D. Fox Superconducting Accelerator Laboratory at Florida State University. The Thick/Thin Target Inverse Kinematics approach [1] was used with a CH_2 target and a radioactive ^{8}Li beam. In this approach, the thick target causes the beam to lose energy as it passes through, allowing a single beam energy to probe a range of reaction energies. To provide a unique event identification, the target is still thin enough for the heavy recoil to leave the target with enough energy to be detected in coincidence with the light recoil.

The ^{8}Li radioactive beam was produced from the ^{2}H(^{7}Li, ^{8}Li)^{1}H neutron transfer reaction. The primary ^{7}Li beam was accelerated with the 9 MV FN tandem Van de Graff accelerator followed by a linear accelerator booster. The target for the primary beam was a deuterium gas cell that was cooled with liquid nitrogen. The resulting ^{8}Li was selected by momentum, bunched and then separated from contaminants with the electromagnetic elements of RESOLUT. The final ^{8}Li beam had a 5% ^{7}Li contaminant from the primary beam. The typical intensity of the ^{8}Li secondary beam was $\approx 2 \times 10^{4}$ pps. The target thicknesses and secondary beam energies allowed for an excitation

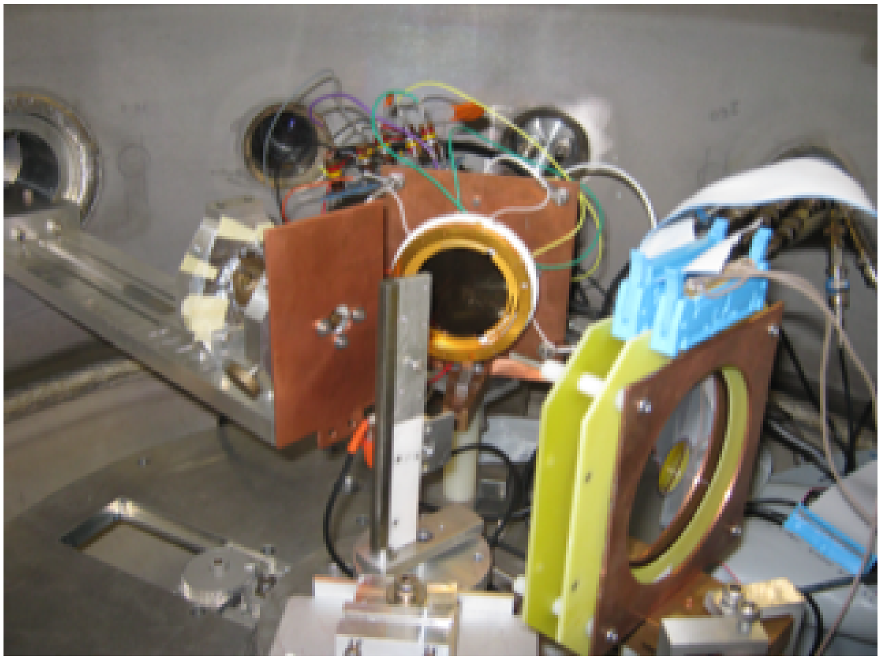

Figure 3.2: S2 detectors in the ΔE-E configuration. This configuration was only used for a single set of runs to achieve an identification of the light recoils.

function for the ^{8}Li+p resonance elastic scattering in energy range of 1.0-2.8 MeV in c.m. to be measured.

3.3.1 Setup

Annular, 500-μm-thick silicon strip detectors (S2) were used for charged particle detection. In the general setup, there were two detectors, one placed 7.6 cm from the target and the other placed at 26.8 cm from the target as in Figure 3.3. The upstream detector was used for detecting light recoil particles while the downstream detector was used to detect heavy recoil particles. With this arrangement, the entire kinematics of the reaction could be determined. The VME-based DAQ system was set to trigger only if the two S2 detectors were in coincidence within a 100 ns time window. A secondary arrangement used a thinner, 65 μm, detector in front of the upstream detector for a ΔE-E arrangement as in Figure 3.2 and Figure 3.4. This second arrangement provides a clean particle ID using the ΔE-E technique and was used in one short run only to verify the event identification described in the next section. These detectors were calibrated with a ^{228}Th source.

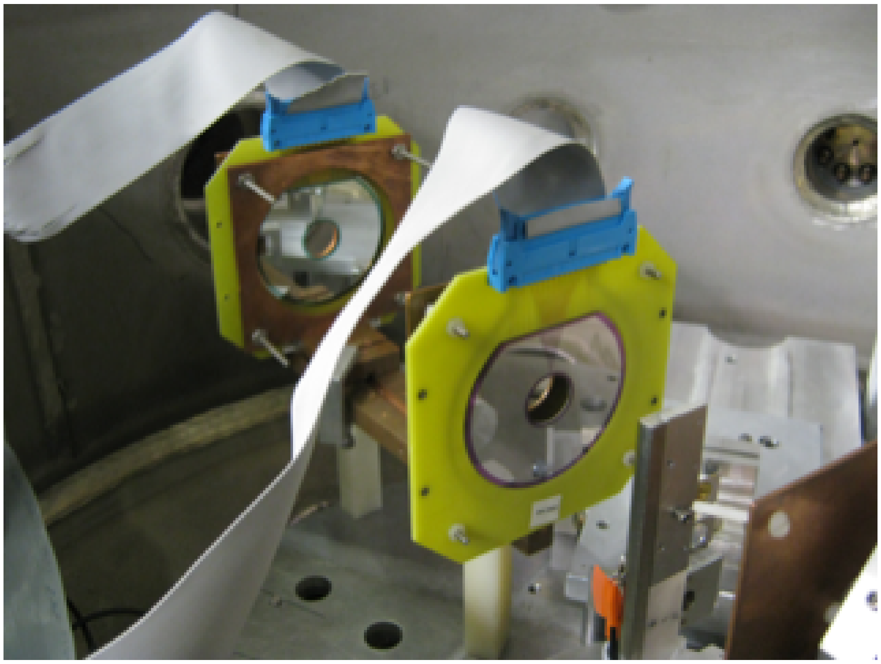

Figure 3.3: After identification of the light recoils, the ΔE detector was removed and the remaining two S2 detectors were moved upstream to reduce scattering events coming from the direct beam. This configuration was used for the remainder of the runs.

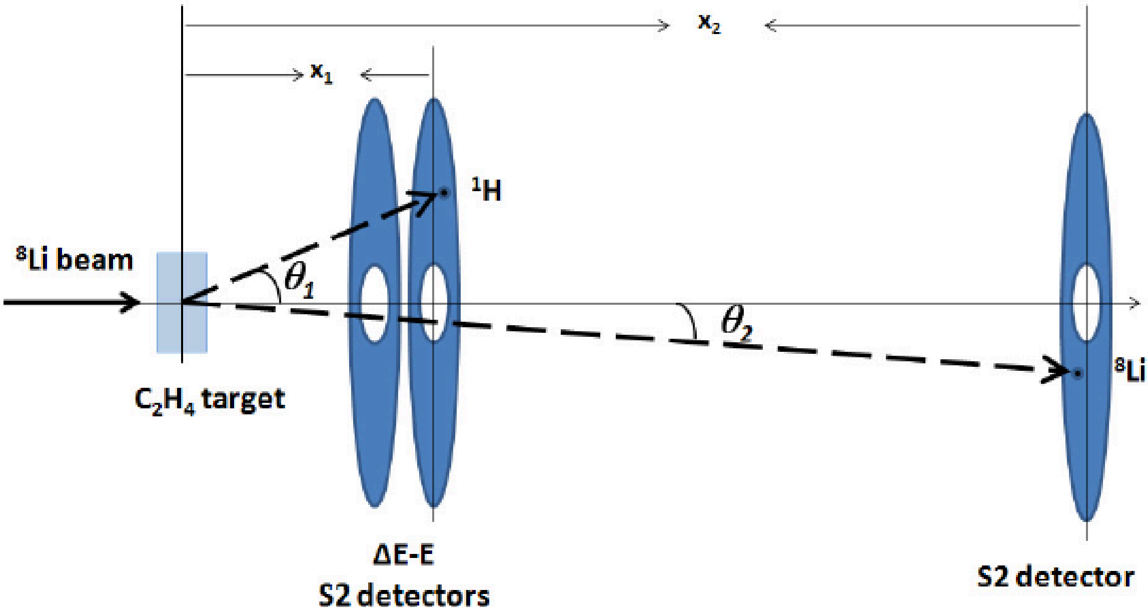

Figure 3.4: Schematic view of the experimental setup used in the ^{8}Li+p experiment for the runs that had the ΔE S2 detector. This detector was later removed and the remaining two S2 detectors were moved upstream to optimize the geometry.

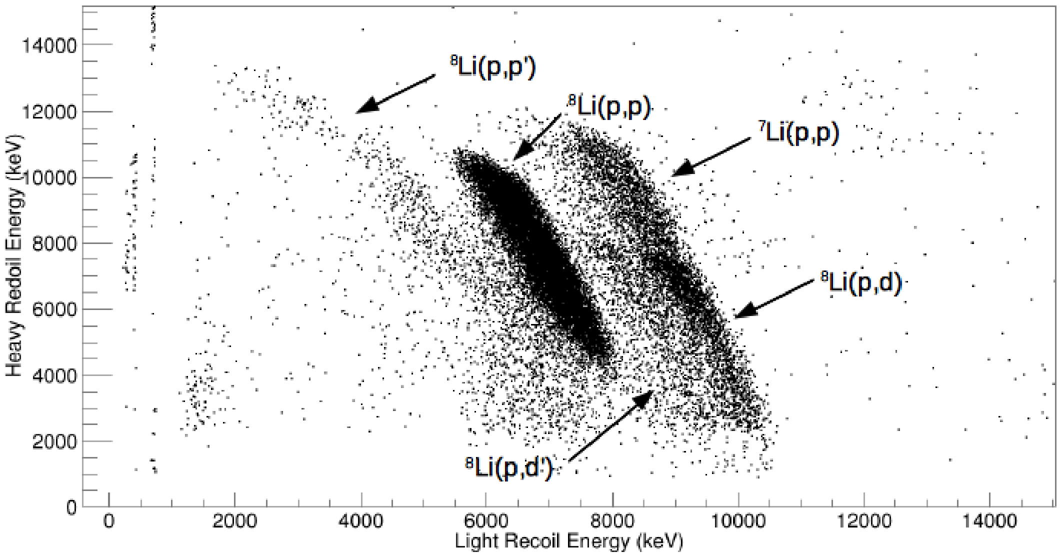

Figure 3.5: The energy deposited in the heavy recoil detector plotted against the light recoil detector. The different reactions are noted. Importantly, the ^{8}Li(p,p) can be isolated with a simple graphical cut.

3.4 Analysis

The ^{8}Li+p elastic scattering is only one of several channels open at the center of mass energies measured (< 3 MeV). Other reactions with significant cross section are inelastic scattering populating the first excited state of ^{8}Li (threshold of 980.8 keV c.m.) and the (p,d) nuclear transfer reaction populating the ground state and first excited state in ^{7}Li with Q-values of 191.95 keV and -285.0 keV respectively. Due to primary beam leaking through, ^{7}Li+p elastic scattering was another reaction that was expected to appear. To identify the reactions, the energy of the light and heavy recoil were plotted against each other in Figure 3.5. The different kinematics of the reactions caused each reaction to be distinct. A graphical cut was able to separate the ^{8}Li elastic scattering events from all other reaction channels.

The intensity of ^{8}Li ions was measured every time the beam energy or target was changed. This was correlated with the trigger rate in the data files for normalization. The normalization was confirmed by using events from the ^{8}Li(p,d)^{7}Li reaction that could be separated from ^{7}Li+p elastic

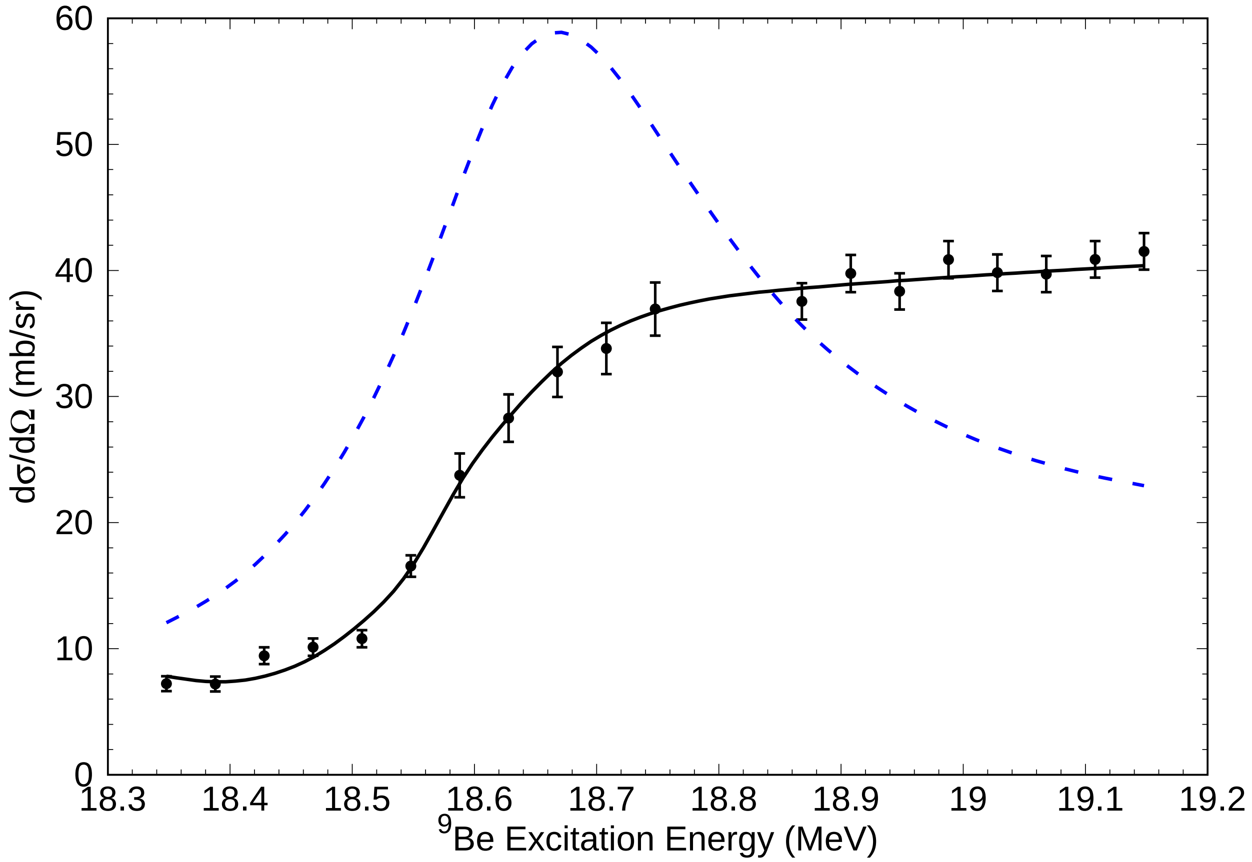

Figure 3.6: Excitation function for ^{8}Li+p elastic scattering for an angular range between 138° and 155° in c.m. The solid curve is the best R-matrix fit with T=3/2 $5/2^{-}$ at 18.65 MeV and T=3/2 $5/2^{+}$ at 18.5 MeV states in ^{9}Be with parameters shown in Table 3.1. The blue dashed curve is the R-matrix calculation with the T=3/2 $5/2^{-}$ state at 18.65 MeV only.

scattering in Figure 3.5 and comparing the resultant cross section to [42]. The excitation function for the ^{8}Li+p elastic scattering is shown in Figure 3.6. It was obtained by selecting only those events that correspond to the kinematics of the elastic scattering, as shown in Figure 3.5. This excitation function is for center of mass angles $138°$-$155°$ and is corrected for the solid angle of the active region seen from the target. The smallest and largest angles of the detectors were excluded to avoid shadowing effects of the first and the second detector.

3.5 R-Matrix Calculation

Analysis of the excitation function for ^{8}Li+p elastic scattering was performed with the R-matrix code MinRMatrix [43]. As was mentioned in the introduction section, some spectroscopy information on the level structure of ^{9}Li, ^{9}C, and T=3/2 states in ^{9}Be in the relevant energy region is available. Therefore, many R-matrix parameters can be fixed *a priori* for this system. Two T=3/2 states at 14.3922 and 16.9752 MeV are well known in ^{9}Be [37]. These are the IAS of the ground (3/2^{-}) and the first excited (1/2^{-}) states of ^{9}Li and ^{9}C. Note that these states are very narrow - 380 eV each [37]. This is because the isospin-allowed nucleon decay channels are energetically forbidden and the resonance widths are dominated by small isospin violating admixtures. The third T=3/2 state is a tentative 5/2^{-} at 18.65(5) MeV [37] and it is a rather broad resonance ($\sim$300 keV) because the isospin allowed proton and neutron decays are open for this state (see Fig. 3.1). There is a good reason to assume that the 5/2^{-} spin-parity assignment is correct. The 5/2^{-} state in ^{9}C has been clearly identified at an excitation energy of 3.6 MeV and well characterized as nearly a single particle state in three recent experiments [30, 40, 5]. Therefore, one is justified to use a simple potential model to predict the Thomas-Ehrman [44] shift between the T=3/2, A=9 isobars for this state. Using conventional parameters for the Woods-Saxon potential with R=1.25$\times 8^{\frac{1}{3}}$=2.5 fm and $a = 0.65$ fm and adjusting the depth to reproduce the 3.6 MeV excitation energy of the 5/2^{-} in ^{9}C, one gets an excitation energy of 5/2^{-} in ^{9}Li at 4.26 MeV. This is less than 40 keV different from the known tentative 5/2^{-} state at 4.296 MeV in ^{9}Li [37]. Using excitation energies of the 5/2^{-} in ^{9}Li and ^{9}C, an excitation energy of the T=3/2 5/2^{-} IAS in ^{9}Be can be estimated at 18.5 MeV. Therefore we expect to observe a single-particle T=3/2 5/2^{-} state in the measured excitation energy region - between 18.35 and 19.19 MeV. Moreover, its R-matrix parameters can be tightly constrained by the fact that neutron decay to the T=0 states in ^{8}Be should be strongly suppressed due to the isospin conservation. The reduced widths associated with these decays were set to zero. The reduced widths for neutron decay to the isospin mixed T=0+1 states at 16.626 and 16.922 MeV in ^{8}Be and proton decay to ^{8}Li(g.s.) are defined by the isospin Clebsch-Gordan coefficients, the nearly unity spectroscopic factor of the 5/2^{-} state [30, 5] and the known isospin mixture of the

T=0+1 2^+ states in ^{8}Be [45]. They are given by the equations below:

$$\begin{aligned}
\gamma_p^2 &= S\gamma_{sp}^2\left(C^{1\,\frac{1}{2}\,\frac{3}{2}}_{1\,-\frac{1}{2}\,\frac{1}{2}}\right)^2 && (3.1)\\
\gamma_n^2 &= S\gamma_{sp}^2\left(C^{1\,\frac{1}{2}\,\frac{3}{2}}_{0\,\frac{1}{2}\,\frac{1}{2}}\right)^2 && (3.2)\\
\gamma_{n(16.626)}^2 &= \gamma_n^2 \times 0.4 && (3.3)\\
\gamma_{n(16.922)}^2 &= \gamma_n^2 \times 0.6, && (3.4)
\end{aligned}$$

where γ_{sp}^2 is the single particle reduced width which was set to 1.25 MeV to reproduce the single particle width of a p-wave resonance calculated with the potential model mentioned above at an R-matrix channel radius of 4.5 fm. The boundary condition was set equal to the shift function calculated at the resonance energy. Using considerations above, all R-matrix parameters for the T=3/2 $5/2^-$ state at 18.65(5) MeV in ^{9}Be are constrained.

The R-matrix calculations that include only the T=3/2 $5/2^-$ state at 18.65 MeV are shown in Fig. 3.6 with a dashed blue curve. Parameters for the $5/2^-$ state are given in Table 3.1 and are consistent with [37]. Obviously, the dashed blue curve does not reproduce the experimental data. Rather, one more T=3/2 state needs to be included. A very broad, purely single-particle $\ell = 0$ $5/2^+$ state has been observed in ^{9}C at around 4 MeV excitation energy [5]. Its IAS should be located at around 18.7 MeV in ^{9}Be. The single-particle nature of this state in ^{9}C allows one to fix the spectroscopic factor to unity and calculate the reduced width using Equations 3.1-3.4. To produce the final fit we allowed the excitation energies of the $5/2^+$ and $5/2^-$ states to vary. We also allowed variation of the total width of the $5/2^-$ state but we kept the ratio of the reduced widths fixed, as defined by Equations 3.1-3.4. The best three-parameter fit is shown in Fig. 3.6 as a black solid curve and the best fit parameters are given in Table 3.1. The reduced χ^2 of the best fit is 0.98. The best fit parameters for the $5/2^-$ state are close to the expected values. The excitation energy of 18.5 MeV for the $5/2^+$ state is in agreement with the predictions of the potential model discussed in [5], which works well for the broad $2s_{1/2}$ $\ell = 0$ scattering states in ^{8}B, ^{9}C, and ^{10}N

Table 3.1: Best fit R-matrix parameters for the T=3/2 states in ^{9}Be with channel radius of 4.5 fm and γ_{sp}^2=1.25 MeV. E_{ex} is an excitation energy in ^{9}Be, E_λ is an energy eigenvalue, Γ is a total width and S is a spectroscopic factor. The natural boundary condition is used so that it is equal to the shift function calculated at the resonance energy, making E_λ equal to p+^{8}Li c.m. energy. The parameters that were varied in the R-matrix fit are boldfaced. The remaining values were recalculated based on the values of the boldfaced parameters and Eq. (1)-(4). The spectroscopic factor for the 5/2$^+$ state was set to unity.

J^π	E_{ex} MeV	E_λ MeV	Γ keV	S	γ_p^2 keV	$\gamma_{n(16.626)}^2$ keV	$\gamma_{n(16.922)}^2$ keV
$\frac{5}{2}^-$	18.65(2)	**1.76(2)**	350(40)	1.2(1)	**510(50)**	410	610
$\frac{5}{2}^+$	18.5(1)	**1.6(1)**	1500	1.0	410	330	490

and predicts that the 5/2$^+$ partial wave should peak at around 1.8 MeV of p+^{8}Li c.m. energy (18.7 MeV). The uncertainties for the fitted parameters were established using the Monte Carlo technique, which randomly varied all three fitting parameters simultaneously and accepted only those sets that resulted in χ^2 values within 90% confidence level.

For completeness we note that while proton decay of the T=3/2 states in ^{9}Be to the first excited state in ^{8}Li (1$^+$ at 0.98 MeV) is energetically possible, it is strongly suppressed by the penetrability factors. We have observed events associated with the inelastic scattering (see Fig. 3.5), but the cross section was a factor of 30 smaller, therefore inelastic scattering cannot have significant influence on the elastic scattering cross section and was excluded from the R-matrix fit to reduce the number of free parameters. Also, the 5/2$^-$ state has two sets of reduced widths; one for channel spin 3/2 and one for channel spin 5/2. As it was discussed in [30, 5], channel spin 5/2 should dominate and we have excluded the reduced widths associated with the channel spin 3/2. An excellent agreement between the three-parameter R-matrix fit and the experimental data validates these assumptions.

3.6 Conclusion

The excitation function for ^{8}Li+p resonance elastic scattering was measured in the energy range that corresponds to the range between 18.35 MeV and 19.19 MeV excitation energy in ^{9}Be. The main goal of these measurements was to provide benchmark data to verify the validity of the isospin symmetry considerations and check if the application of the TTIK approach for spectroscopy studies of neutron rich nuclei with rare isotope beams leads to reliable results. The measured excitation function was perfectly described by the R-matrix approach, which included the two T=3/2 states only (5/2$^-$ and 5/2$^+$). Moreover, the best fit reduced widths, total widths, and resonance energies are in agreement with the values expected based on the isospin symmetry considerations and most recent experimental information on the level structure of the T=3/2 A=9 iso-quartet. We confirm that the excited state at 18.65 MeV in ^{9}Be [37] is indeed a 5/2$^-$ T=3/2 IAS. We have also identified a new broad 5/2$^+$ T=3/2 state at 18.5(1) MeV. It appears that the T=1/2 states play only a minor role in this case. This is probably due to the presence of strong, single-particle T=3/2 resonances which dominate the cross section for ^{8}Li+p elastic scattering. It was shown that isospin symmetry considerations are still valid in this case, which features broad states in the continuum. This is encouraging and validates the application of the TTIK method for future spectroscopy studies of neutron-rich nuclei with rare isotope beams, such as the study of ^{13}Be in the next chapter.

4. ^{12}BE + P AT TRIUMF WITH TEXAT

4.1 The ^{13}Be problem

4.1.1 Introduction

The ground state of ^{11}Be is $1/2^+$, and not $1/2^-$, as expected from naive shell model considerations. It is an example of parity inversion, where the shell structure has evolved such that the $1p_{1/2}$ level is above the $2s_{1/2}$ level. The valence nucleons in the ground state of ^{12}Be (^{10}Be+2n) are in the mixed, $1p_{1/2}+2s_{1/2}$, configuration [25]. The ground state spin-parity of ^{13}Be is an open question both theoretically and experimentally. In addition to being of interest to developing structure calculation methods, the structure of the ground state of ^{13}Be is important for understanding the Borromean nucleus, ^{14}Be through the ^{12}Be + n configuration.

4.1.2 Experimental Studies

The experimental study of ^{13}Be has been carried out with a variety of methods over the last 30 years. One of the earliest experimental studies of ^{13}Be was performed in 1992 by A.N Ostrowski *et al.* [7] by measuring the missing mass of ^{13}Be through the ^{13}C(^{14}C,^{14}O)^{13}Be reaction. Two possible states were observed, one at 2.01 MeV above threshold and one at 3.12 MeV above that, with the 2.01 MeV state tentatively given a $5/2^+$ spin-parity assignment based on indirect arguments. Notably, the 2.01 MeV state was claimed to be the ground state, however a lower energy ground state could not be ruled out because the cross section of a low energy $J = 1/2$ state would be too low for their statistics. A similar method of measuring mass excess applied to ^{14}C(^{11}B, ^{12}N)^{13}Be in 1998 by A.V. Belozyorov *et al.* [8] reproduced the 2.01 MeV state but, due to significantly higher statistics, also suggested a ground state at 0.80 MeV above threshold with a spin of $J = 1/2$, however they were unable to make an assertion of the parity due to lower resolution.

Another candidate for the ground state was suggested two years later by M. Thoennessen *et al.* [9] by measuring the neutron decays from an ^{18}O beam fragmented on a ^{9}Be target. Two options for the ground state were able to fit the relative velocity plot of neutrons and ^{12}Be, either a virtual s-wave state with a scattering length of $a_s = -20$ fm (corresponding to an energy of about 60 keV), or a p-wave state at 50 keV. The virtual s-wave ground state was a better fit, though neither option could be ruled out. The 2.01 MeV state from previous studies was once again observed, though insufficient on its own to fit the data. The data measured were not sensitive to the possible 0.80 MeV state.

Most recent experimental studies of ^{13}Be have been performed with the invariant mass method, populating states in ^{13}Be and looking at the relative momentum and energy between the decay fragments, ^{12}Be + n [10, 11, 12, 13, 14]. H. Simon *et al.* [10] looked at the halo nuclei ^{11}Li and ^{14}Be by fragmenting them on a carbon target. The fit to their ^{12}Be + n cross section was done using the familiar 2.0 MeV state, an s-wave virtual state with a scattering length of $a_s = -3.2$ fm, as well as two $1/2^-$ states, one at 0.8 MeV and one at 3.04 MeV. Y. Kondo *et al.* [11] explored the one-neutron removal from the ^{14}Be + p reaction and fit their cross section using a $a_s = -3.4$ fm scattering length virtual s-wave state, a 0.51 MeV p-wave state, and a 2.39 MeV d-wave state. It is notable that the d-wave state was determined to be at 2.39 MeV instead of 2.0 MeV as noted in previous studies. Y. Aksyutina *et al.* [12] also used the ^{14}Be + p reaction but at a much higher energy and suggested a narrow s-wave resonance at 0.44 MeV, a very wide s-wave resonance at 0.81 MeV, the familiar d-wave resonance at 1.95 MeV, as well as a negative parity resonance, $1/2^-$, at 3.0 MeV. G. Randisi *et al.*[13] used ^{14,15}B beams on carbon targets to explore ^{13}Be, by comparing their results to shell model calculations it was suggested that they observed a $1/2^+$ resonance at 0.4 MeV, a $5/2^+$ resonance at 0.85 MeV, and another $5/2^+$ resonance at 2.35 MeV. B.R. Marks *et al.* [14] used nucleon exchange from ^{13}B on a ^{9}Be target where ^{13}Be was produced, immediately decaying to ^{12}Be + n. They determined only a single s-wave resonance at 0.73 MeV and a single d-wave resonance at 2.29 MeV were sufficient to fit their results.

Despite there being many experimental studies on ^{13}Be, a consensus on the structure of the low laying states has yet to be reached. The most agreed-upon structure is the existence of a $5/2^+$ state around 2 MeV. The most recent studies seem to agree that the lowest state is $1/2^+$ very close to threshold, with some casting it as a virtual state and others treating it as a resonance. The existence and properties of any states between these two is up for some debate. Many of the studies suggest a 1/2$^-$ state near the ground state while others suggest there could be another 5/2$^+$ state and some suggest no states at all exist between them.

4.1.3 Theoretical Studies

Some of the earliest calculations of the structure of ^{13}Be were p-shell no-core shell model calculations [15] that determined the ground state of ^{13}Be would be a 1/2$^-$ state 1.16 MeV above the neutron separation energy with a 5/2$^+$ excited state 0.05 MeV above the ground state followed by a 5/2$^-$ 1.28 MeV above ground state and a 1/2$^+$ at 1.55 MeV. Most calculations of the structure of ^{13}Be, however, involve looking at the ^{12}Be + n and ^{12}Be + n + n systems [16, 17, 18, 19]. These calculations construct the Hamiltonian as ^{12}Be + n (+ n) and solve the Schrödinger equation. The results of the calculation are tuned using ^{12}Be + n + n and compared to experimental data for ^{14}Be, the parameters are then applied to the ^{12}Be + n system to determine structure information for ^{13}Be. In some cases, the 5/2$^+$ state is defined to be at 2 MeV in accordance with accepted structure of ^{13}Be from experiment [16]. The ground state in these calculations has been found to be 1/2$^+$ and barely unbound [16, 18] or 1/2$^-$ state at lower energy [17, 19]. The application of antisymmetrized molecular dynamics to look at the N=8 shell closure in ^{13}Be found a low energy 1/2$^-$ ground state below a 5/2$^+$ excited state [20].

4.1.4 Conclusion

Both experimental and theoretical studies give many different answers to the question of what the structure of the low-lying states in ^{13}Be are. It is generally accepted that there is a 5/2$^+$ state at 2.0-2.4 MeV above the neutron separation threshold. The ground state is likely to be less than 1.0 MeV above threshold with a spin of $J = 1/2$ but the parity is the subject of some debate. There is some evidence to suggest other states may exist between the ground state and the 5/2$^+$ state, such as a negative parity state in the case of a positive parity ground state or another 5/2$^+$ state, but it is far from conclusive. Studying the isobaric analogue to the low laying states of ^{13}Be in ^{13}B could

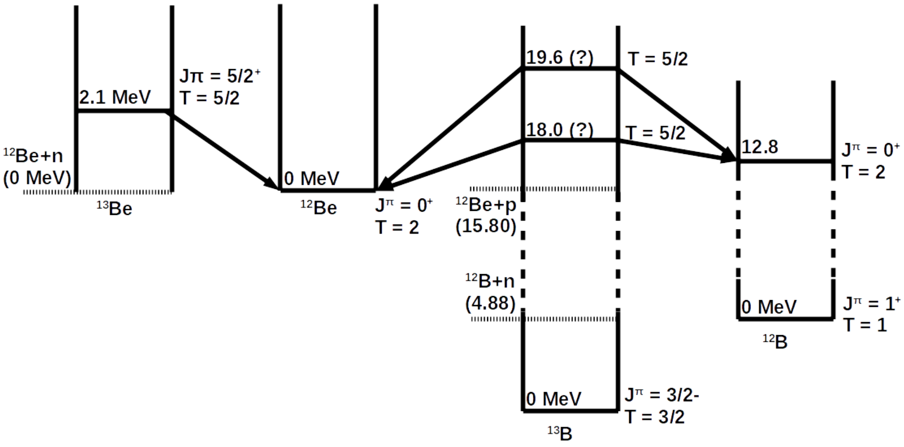

Figure 4.1: A partial level structure and decay channels of ^{13}Be and ^{13}B. [22, 23]

answer the question of what the ground state structure of ^{13}Be is. ^{12}Be+p elastic scattering would populate the low laying A=13, T=5/2 states in ^{13}B. One advantage would be a potential s-wave ground state would no longer be virtual if populated with protons. Thus the technique developed with the ^{8}Li+p experiment could be used with ^{12}Be+p to determine what the spin and parity of the ground state of ^{13}Be is, in addition to other states in the measured region.

4.2 Texas Active Target (TexAT) detector

4.2.1 Overview

Measurements were performed using the Texas Active Target (TexAT) detector, shown in Figure. 4.2 [46]. As a Time Projection Chamber (TPC), TexAT uses a highly-segmented Micro-MEsh GAseous Structure (Micromegas) detector to track particles in the chamber. For additional amplification a Gas Electron Multiplier (GEM) is placed before the Micromegas mesh. Tracks of the beam particle and the heavy and light recoil particles are recorded by the TPC. As an active target TPC, TexAT uses the gas as a target for scattering studies. In TexAT, an array of Si detectors are placed at the forward wall of the chamber backed by CsI crystal scintillators to measure the energy

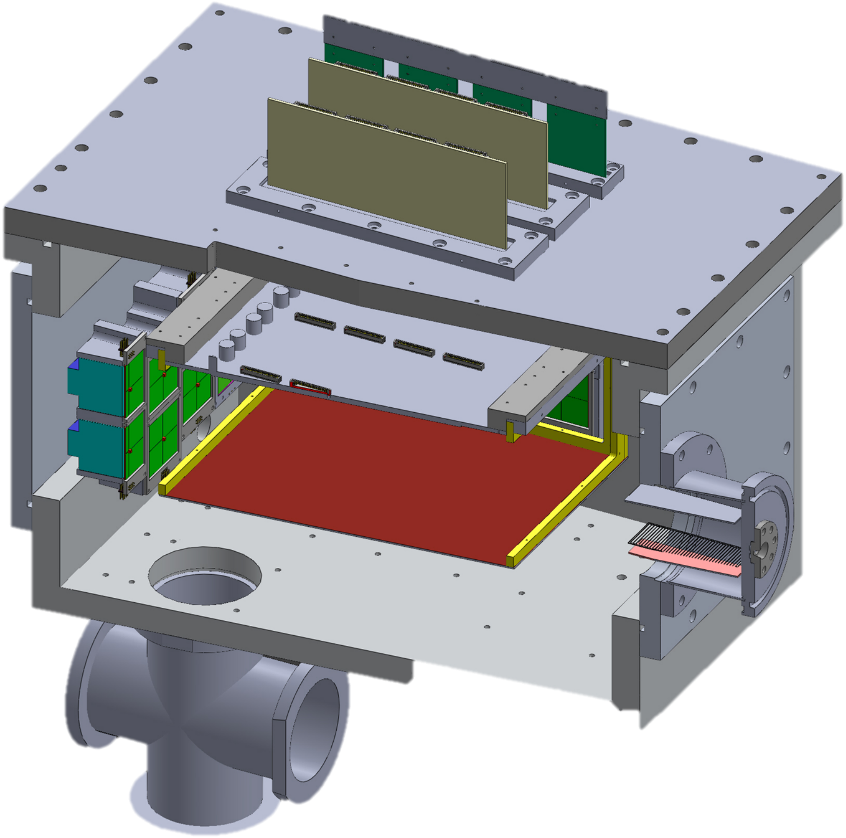

Figure 4.2: Cutaway of TexAT showing the Micromegas plate, Si/CsI detector wall at the back and ionization chamber.

of the light recoil particles. The particle tracks in the detector are used to reconstruct the reaction kinematics in conjunction with the total energy measurements in the Si and CsI detectors. An ionization chamber, located after the upstream window, is typically used to count the number of beam particles entering the chamber for normalization. Due to poor performance of the ionization chamber during the experiment, the signal on the GEM was used to count beam particles.

4.2.2 Time Projection Chamber

The TPC in TexAT consists of a segmented Micromegas detector, at the top of the chamber, and a field cage surrounding the gas-filled active volume. The field cage surrounds the perimeter of the active volume with resistor separated wires, defining a uniform electric field between the copper plate cathode at the bottom of the active volume and the Micromegas mesh anode at the

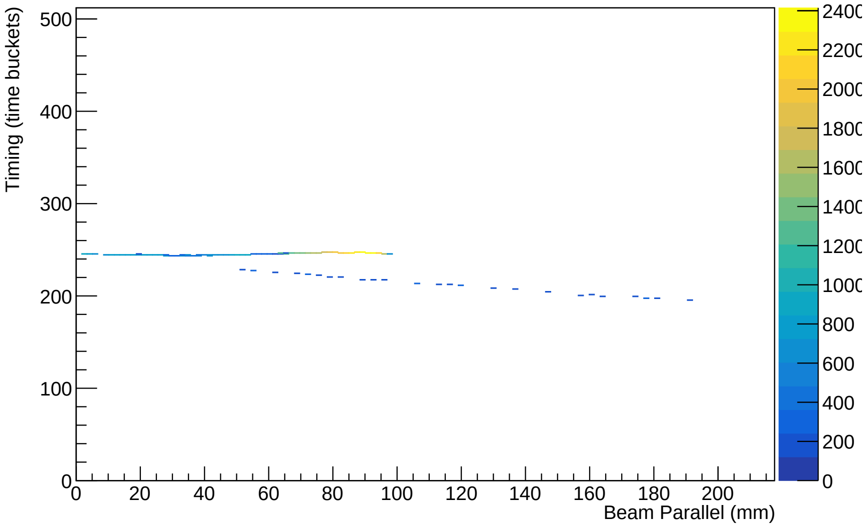

Figure 4.3: Time vs position in the Micromegas with the timing of the signals on the y-axis and the position in the TPC along the beam axis on the x-axis. Timing gives a very good determination of the vertical position of the particles in the TPC. In this case there is a heavy recoil particle continuing mostly forward and a light recoil particle moving off at an angle upward (lower time corresponds to positions closer to the top micromegas plate).

top. The field cage covers and area of 316 mm × 346 mm with a distance between the cathode and anode planes of 135 mm. Within the active region, electrons ionized in the gas drift to the Micromegas plate, the drift speed is determined by the field strength of the field cage, the gas, and the gas pressure. By measuring the arrival time of the electrons at the Micromegas, the position of the particle in the vertical direction can be determined as seen in Figure 4.3.

4.2.2.1 Micromegas

Micromegas detectors are gas-electron amplification devices [47] that consist of an anode plane, a cathode plane, and a micromesh plane very close to the anode plane as diagramed in Figure 4.4. In TexAT the distance between the mesh and anode planes is 128 μm. With a sufficiently strong potential difference between the mesh and the anode, electrons entering the Micromegas will create an avalanche of electrons, providing gains on the order of 10^3. The amount of gain is related to the potential, the type of gas, and the gas pressure. Generally, lower pressure provides

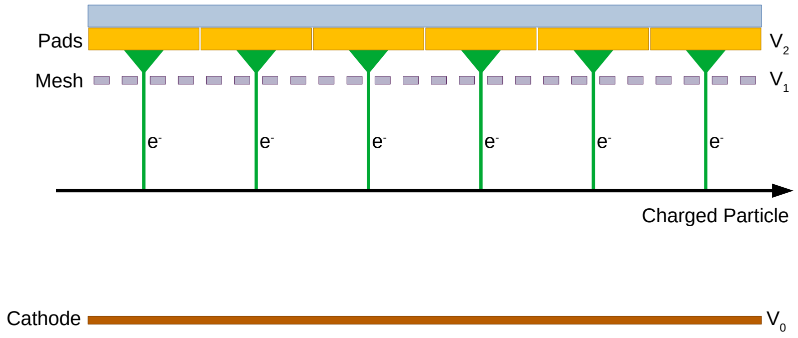

Figure 4.4: A diagram of a Micromegas detector (not to scale). As charged particles move through the TPC region the gas is ionized and electrons drift up toward the micromesh and readout pads due to the potential between the cathode and the mesh. When the electrons drift in between the mesh and pads, the higher potential gradient causes the electrons to ionize the gas, creating an avalanche of electrons to be captured by the pads.

higher gains as a longer mean free path for the electrons allows them to gain more energy between collisions improving the chances of generating more electrons.

The Micromegas in TexAT has an active region that is 224 mm along the beam axis and 245 mm perpendicular to the beam axis. The active region is split into three separate sections: beam left, beam right, and beam center as shown in Figure 4.5. The beam center region runs along the beam axis and is segmented into 6 columns of 128 rows of 1.67 mm × 3.42 mm pads. The left and right regions are identical and are segmented in a strip and chain arrangement. The segmentation of the Micromegas can be seen in the picture of the Micromegas plate in Figure 4.6. The side regions are split into 128 rows of pads perpendicular to the beam axis, every other row is a single pad 1.67 mm × 101.5 mm in dimension called a "strip." The remaining rows are split into 64 segments, 1.67 mm × 1.67 mm in dimension, which are connected into "chains" parallel to the beam axis. By correlating the timing of the signal measured in the strips and chains a particle track can be resolved as shown in Figures 4.7 and 4.8.

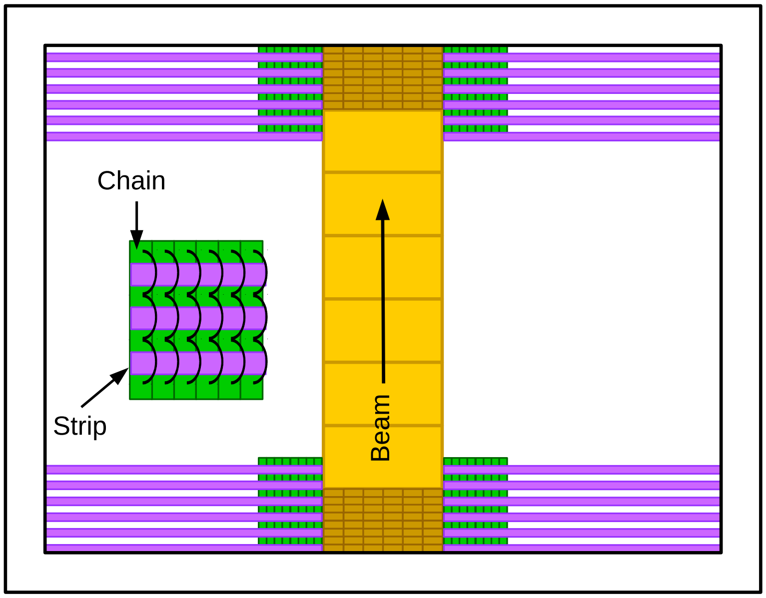

Figure 4.5: A diagram of the multiplexing for the TexAT Micromegas. The central region, shown in gold, is segmented into 8 subsections each further segmented into 8 rows of 6 pads. The side regions use a strip and chain configuration with long pads known as strips in purple and chains of pads in green. The pads in each chain are linked together, effectively creating pads that run the length of the plate.

Figure 4.6: A close up picture of the Micromegas plate in TexAT.

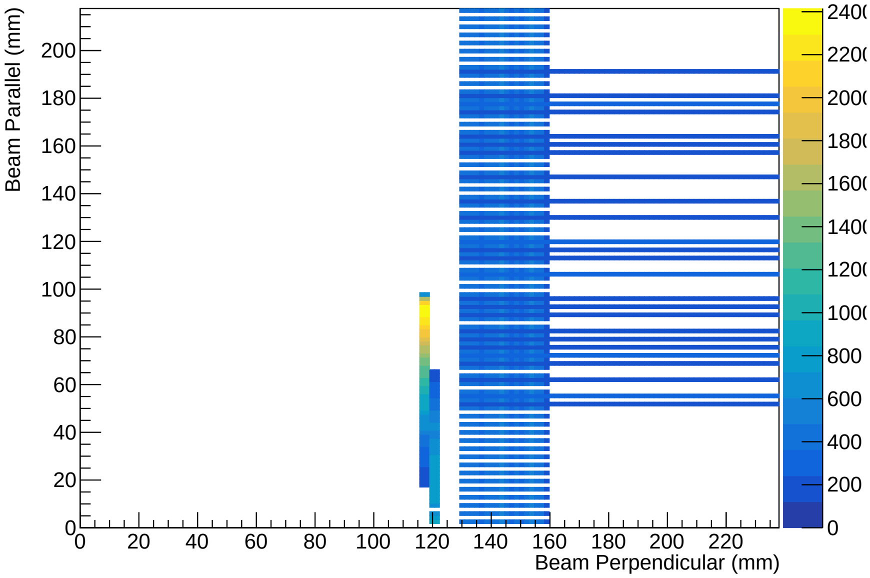

Figure 4.7: A raw track measured by the Micromegas displayed as the energy deposited in each pad that fired for the area of each pad. The multiplexing of the strips and chains can be seen clearly on the right side.

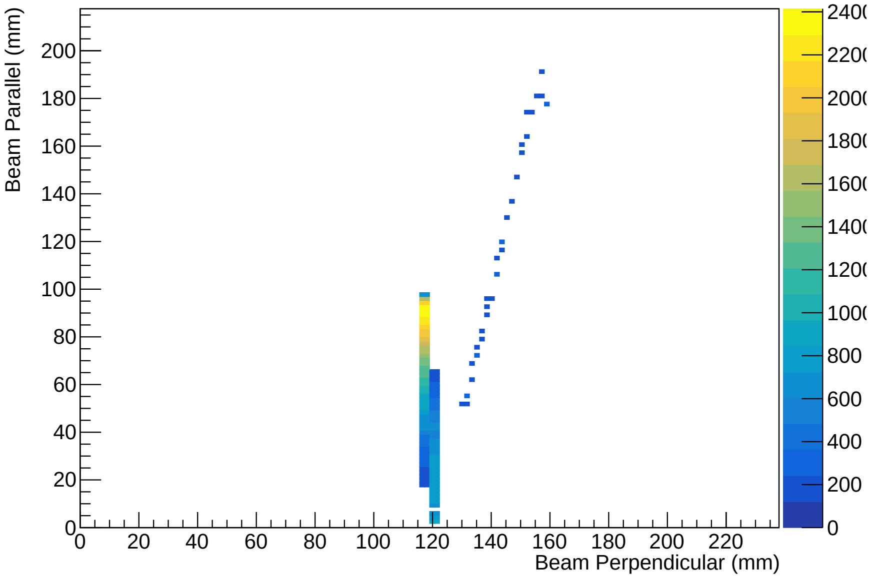

Figure 4.8: The cleaned track from Figure 4.7 using the timing of the signal. The signals in the strips and chains have been localized to the positions where the timing of the strips and chains correlate.

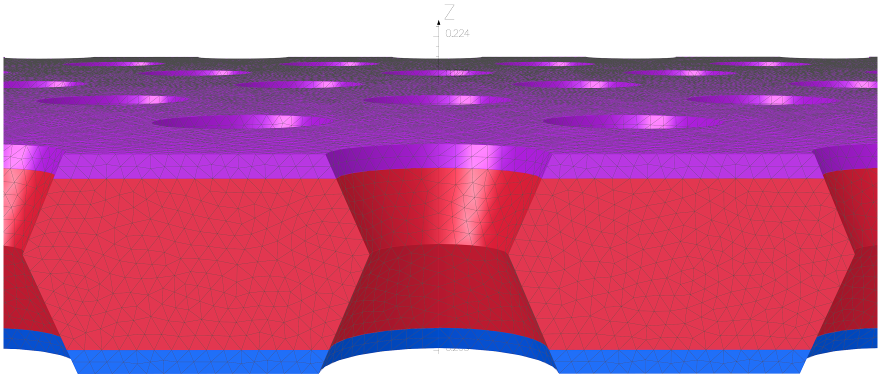

Figure 4.9: Cross section of a 3D model of the GEM used in TexAT. Electrons are funneled into the holes where they ionize the gas creating more electrons. E. Galyaev, RDI Technologies LLC, Private Communication.

4.2.2.2 GEM

GEMs are gas-electron amplification devices, similar to Micromegas, that consist of a thin polymer foil coated in metal on both sides and containing a high density of holes [48]. A cross section of a model of the GEM used in TexAT is shown in Figure 4.9. By applying a high potential between the foil a large electric field is created and electrons drift toward the holes. As electrons pass through the holes, they ionize the gas and create an avalanche of electrons, the majority of which leave the GEM. Placed before the Micromegas detector in TexAT, the GEM provides additional gain to what the Micromegas already produces. The GEM used in TexAT is 2 mm thick with a hole spacing of 140 μm. In TexAT, the charge collected on the electrodes can be measured for diagnostic purposes. Within this experiment this feature was utilized to count the number of beam particles entering the chamber as every particle would produce a signal.

4.2.3 Solid State Detectors

TexAT has the option of including Silicon/Cesium-Iodide telescopes for detection of charged particles (see Figure 4.10). In the full configuration TexAT can have 50 Si/CsI telescopes, surrounding the active region on five sides (the Micromegas plate is on the sixth side). In the configuration used in this experiment, only the downstream wall had Si/CsI telescopes. The downstream

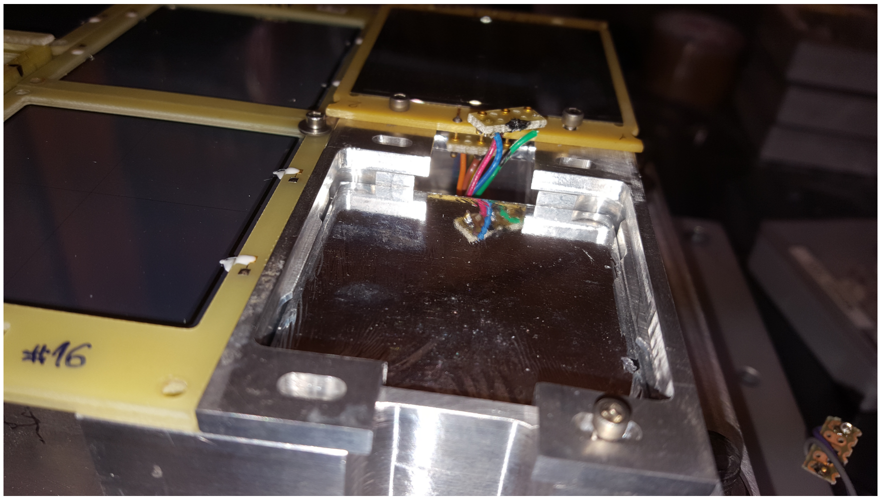

Figure 4.10: Picture of the solid state detector telescopes with one Si detector removed to show the CsI detector behind it.

wall can have two rows of 5 telescopes, for a total of 10, with the central pair of detectors offset to provide a detector at 0° (see Figure 4.11). These detectors are used to measure the energy of recoil particles in scattering experiments and can provide identification for particles that have sufficient energy to "punch through" the Si detector.

4.2.3.1 Silicon Detectors

There are three different types of Si detectors used in TexAT, all of which have active region dimensions of 50 mm × 50 mm. In the 0° position, blue in Figure 4.12, is a W1-500 detector from Micron Semiconductors. The W1-500 is a 500 μm thick detector with 16×16 segmentation with 16 vertical strips on the front and 16 horizontal strips on the back. This segmentation provides additional position sensitivity for particles near 0°. The green coded detectors in Figure 4.12 are 635 μm thick, KDP-1K Si detectors developed at the JSC "Institute in Physics-Technical Problems", Dubna, Russia for TexAT. The front side is made of four 25 mm × 25 mm segments while the back is a single 50 mm × 50 mm segment. The remaining positions (red in Figure 4.12) are filled with MSQ25-1000 detectors from Micron Semiconductors. Similar to the KDP-1K detectors, the MSQ25-1000 detectors have a 4 segment front side and a single segment backside. The MSQ25-1000 were the thickest detectors, being 1 mm thick.

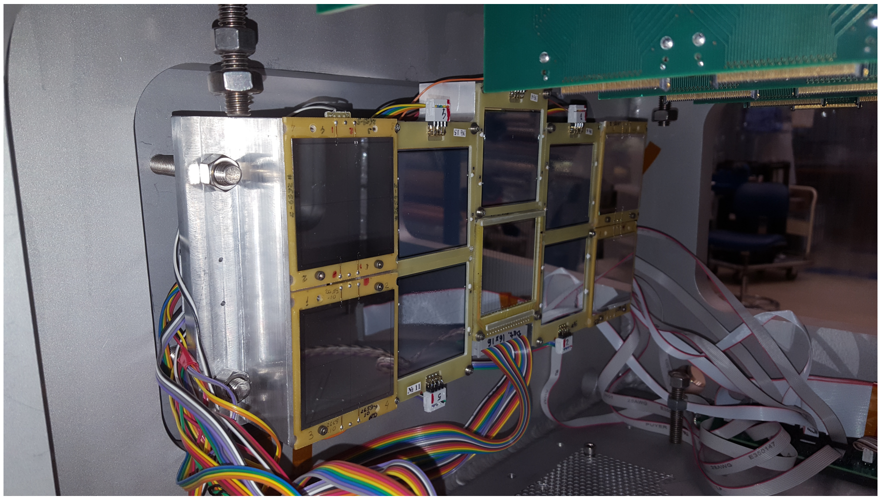

Figure 4.11: Picture of the solid state detector telescopes inside the TexAT chamber with the TPC removed, showing the configuration of the detectors.

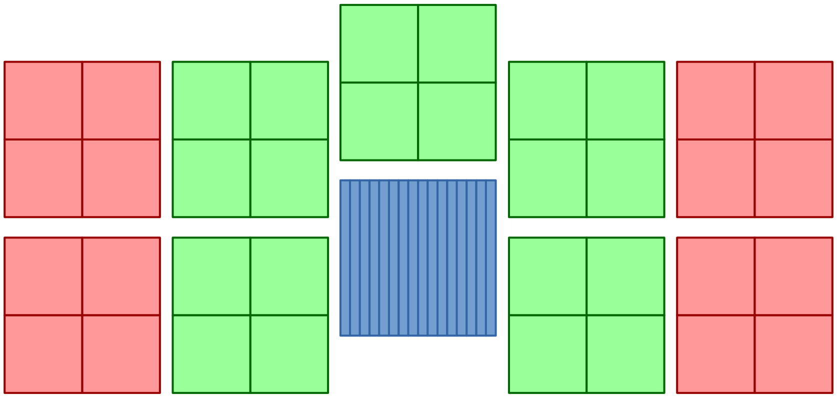

Figure 4.12: Diagram of the arrangement of the different types of Si detectors. The blue detector is the 16x16 detector, the green is the 500-μm-thick Dubna detectors, and the red are the 1-mm-thick Micron detectors.

4.2.3.2 CsI Detectors

The CsI detectors in the Si/CsI telescopes serve to measure the energy remaining for particles that have sufficient energy to punch through the Si detectors with good energy resolution (about 5%). Their cross section is 50 mm × 50 mm to match with the Si detectors and their thickness is 40 mm, allowing them to measure the energy of charged particles or gamma rays, though the later function was not utilized in this experiment. Each crystal is wrapped in aluminized mylar and has an attached preamp which reads out a Hamamatsu S3204 PIN diode.

4.2.4 General Electronics for TPCs (GET)

The TexAT TPC has 1024 channels, the Si detectors have a total of 77 channels, and the CsI detectors add an additional 10 channels for a total of 1111 channels. To read out such a large number of channels, General Electronics for TPCs (GET) is used [49]. The GET system uses several different modules to perform the various tasks involved in signal readout. The first module, the AGET chip, gathers the data for up to 64 channel and has a built in pre-amplifier and shaper. An additional 4 channels, fixed-pattern noise (FPN) channels, are provided that do not carry data but otherwise are identical to the other 64 and give a measure of the electronic fluctuating baseline as a function of time. The integration time of the AGET shaper is too short to handle the slow (5 μs) CsI detector signals. Additionally, the CsI detectors used in TexAT have built in pre-amplifiers. Therefore, the AGET pre-amplifier and shaper are bypassed for the CsI detectors, and an external Mesytec MSCF-16 shaper with 4 μs integration time is used instead.

AsAd boards contain four AGET chips and digitize signals from the AGET chips using on board analog-to-digital converters. TexAT uses four AsAd boards for the Micromegas and additional boards for the Si detectors, CsI detectors, and other detectors and signals that need to be recorded. The digitized signals from the AsAd boards are collected by CoBo boards, which can handle up to four AsAd boards. The CoBo boards collect and send the data to be stored, with a time stamp, when a trigger is received. To work with multiple CoBo modules, a MuTAnt module is needed to synchronize the CoBo boards. GET can use several trigger modes: external, internal by

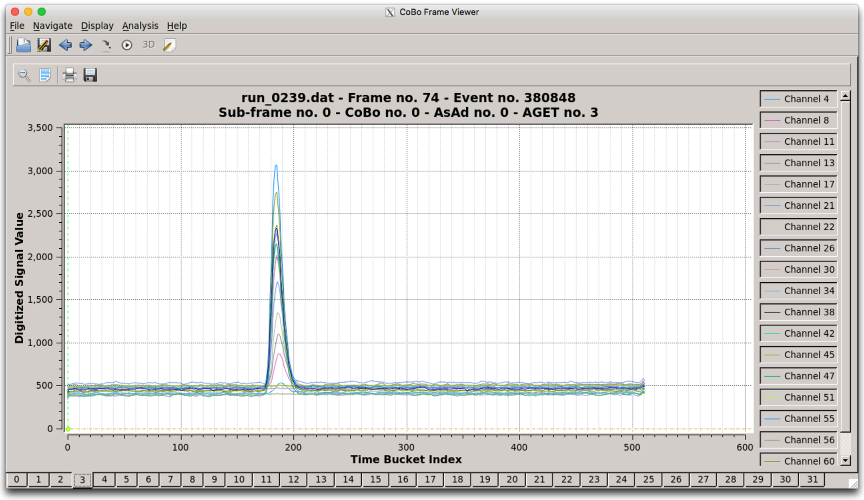

Figure 4.13: The waveforms for 1/8th of the central region of the Micromegas showing particles moving through the section of the TPC.

summing the multiplicity triggers of the CoBos, and a trigger on a predefined pattern of channels. The output of the GET system is a .mfm file which stores the waveforms for all channels that fired as seen in Figure 4.13.

4.3 Experiment

The study of ^{12}Be + p was performed at TRIUMF (British Columbia, Canada) using the ISAC-II facility [50]. The ISAC facility at TRIUMF is used for the production of radioactive ion beams using the isotope separation on line (ISOL) method. Core to ISAC, and TRIUMF in general, is a H^- cyclotron producing 500 MeV protons at up to 100 μA. These protons are then bombarded on a target, producing radioactive isotopes. The radioactive isotopes are mass separated and sent through a series of room temperature accelerators in the ISAC-I hall. The first of these accelerators is a radiofrequency quadrupole (RFQ) accelerator, which is used to inject particles into the next stages. At the exit of the RFQ, a thin carbon foil increases the charge state of the ions. These ions are transported into the next accelerator, the drift tube linac (DTL). For experiments using the ISAC-II experimental hall, the DTL directs ions into the ISAC-II superconducting linac (SC-linac). The SC-linac is comprised of eight cryomodules, each with four to eight superconducting cavities

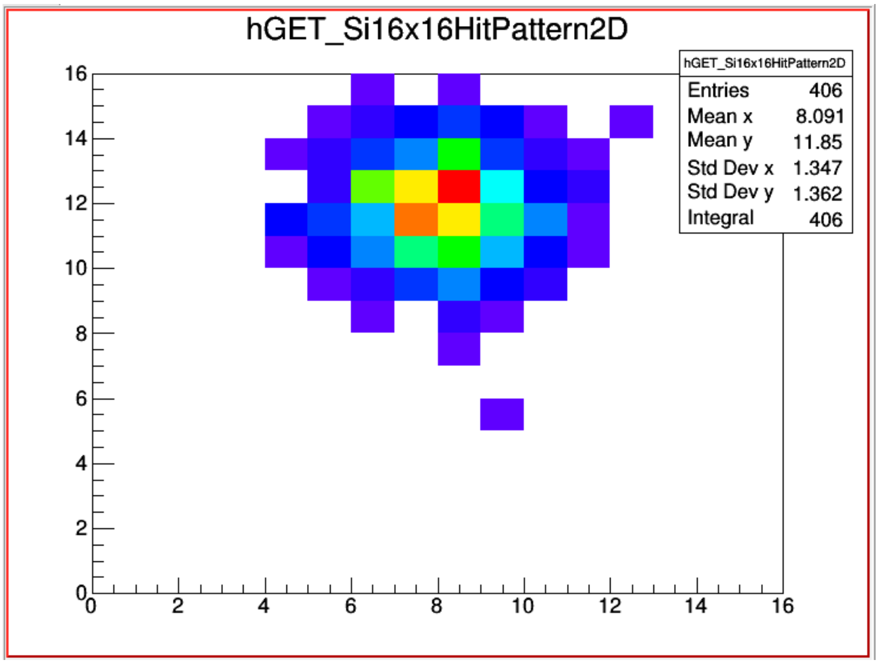

Figure 4.14: The image of the ^{12}C pilot beam on the 0° si detector. The position of the beam spot corresponds to the center of the chamber. The x-axis is the horizontal position on the detector and the y-axis is the vertical position on the detector. Each bin represents a single front/back strip combination. The beam position being off center of the detector vertically is due to the detector being off center vertically in the setup.

and one superconducting solenoid, and can accelerate ions up to 16 MeV/u.

For this experiment, the ISAC-II experimental hall was used. ^{12}Be ions were produced from a tantalum target and accelerated through the ion transport system to the SC-linac. The SC-linac accelerated the ^{12}Be ions to 6 MeV/u. This energy allowed the measurement of the excitation function in the center of mass frame starting from 6 MeV down to 1 MeV. This corresponds to the excitation energy region in ^{13}B where low-lying T=5/2 isobaric analogue states are expected (see Figure 4.1). A ^{12}C beam was used for beam alignment into TexAT with the 0° Si detector used to measure the beam spot as shown in Figure 4.14.

To measure the ^{12}Be(p,p) reaction, TexAT was filled with 260 Torr of isobutane gas which was used as a proton target. This gas pressure was tuned such that the ^{12}Be beam would stop before the last 1/8 of the active region of the TPC, shown in Figure 4.15. The TexAT micromegas were divided into two gain regions, a low gain region for the beam and heavy recoil, and a high gain region sensitive to protons. The low gain region was the first 7/8 of the high segmented central region. The high gain region was the side strip and chain regions and the last 1/8 of the segmented central region, necessitating the beam stopping before this region. The potential on the Micromegas mesh was set to -10 V while the low gain region anode had a potential of 370 V and the high gain potential was 460 V. The potential for the high gain region on the Micromegas was limited by the electronics, causing current spikes at higher potentials, possibly indicating sparking. For the GEM a constant gain was used, with potentials of -410 V and -70 V. Ordinarily the ionization chamber, placed inside TexAT, would count and identify incoming beam particles. With the gas and pressure used, however, the ionization chamber was unreliable and the signal read off one of the GEM layers was used instead for a count of beam particles. Identification of beam particles was not a priority due to the high purity of ^{12}Be beam coming from ISAC-II, which we estimate to have less than 1% contamination from ^{12}C as discussed below. Events were triggered by hits in the Si detectors since only events where the energy of the light recoil particles could be measured were of interest. Because ^{12}Be has a lifetime of 21.47 ms and decays entirely by beta decay, the majority of triggered events were beta particles from the beam particles stopped in the gas.

4.4 Analysis

4.4.1 Analysis Libraries and Event Viewer

The data from the GET DAQ used with TexAT consists of the waveforms recorded per event and sorted by CoBo, AsAd, AGET, and channel numbers. To analyze this data, the waveforms must be processed into energy and time. Due to the complex nature of the TexAT TPC further processing is required to acquire tracks. A set of ROOT-based libraries were produced to map the channels to detectors, process the waveforms, manage events, and process tracks. Additionally a Graphical User Interface (GUI) was written using these libraries for making the viewing of events more readable and to provide diagnostics for the libraries.

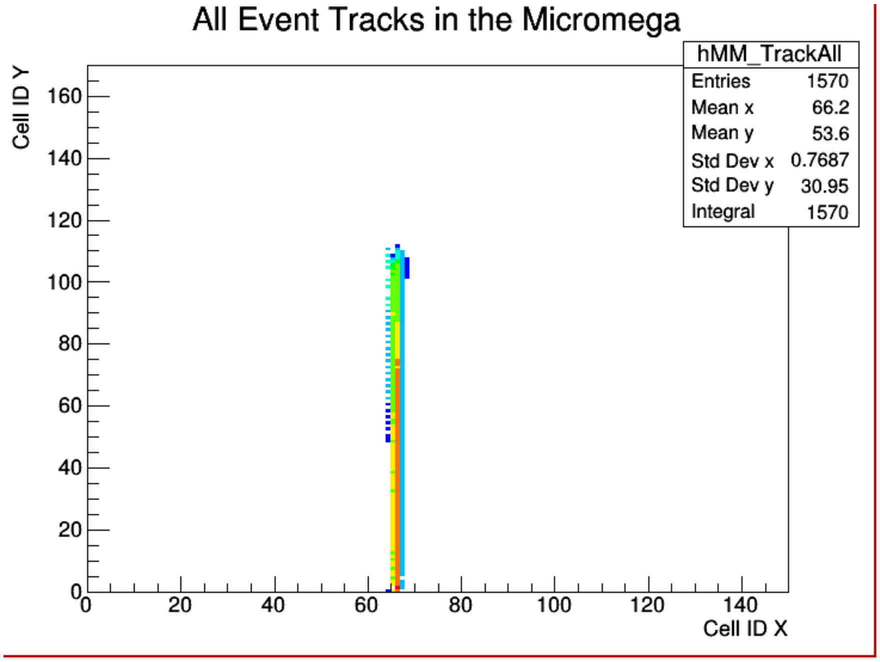

Figure 4.15: The track of the ^{12}Be beam stopping in the TPC before the final 1/8th of the active region of the Micromegas.

4.4.2 Waveform processing

The waveforms recorded by GET have a maximum channel of 4096 and 512 time buckets consisting of 40 ns each. The first step of processing the waveforms is to subtract the average of the FPN channels from the waveform. As mentioned above, the FPN channels are four channels on each AGET chip that do not carry data, thus serving to measure the electronic noise present. By averaging the FPN signals and subtracting them from the waveforms this noise can be mitigated. The next step is to correct the polarity of the front side of the Si detectors and the CsI detectors, these channels have a negative polarity and must be inverted. The polarity of the different waveforms can be seen clearly in the waveform snapshot of an event in Figure 4.16. From here the baseline subtraction is performed. The baseline is measured by taking the average of time buckets 21 through 29; a range at the end of the 512 time bucket range could not be included due to the width of the CsI waveforms. A comparison of the raw and processed waveforms is shown in Figure 4.17.

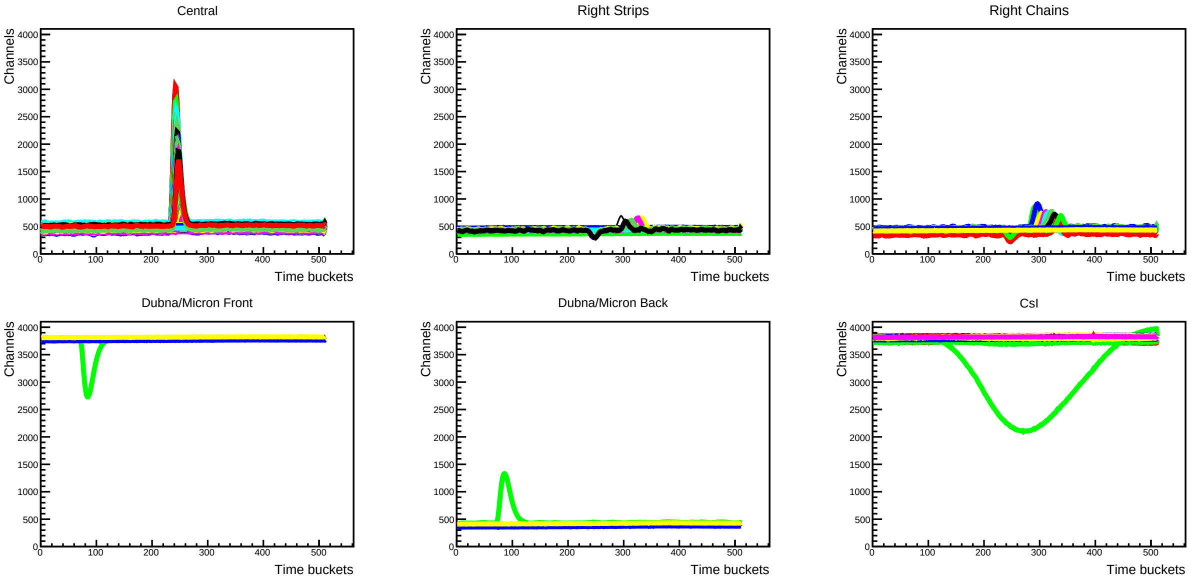

Figure 4.16: The waveforms for a single event. The top row are the waveforms for the micromegas separated into central region, strips, and chains. For the micromegas many waveforms will be recorded and all are plotted here with each channel arbitrarily colored to keep them distinct. The bottom row has the Si detectors front and back and the CsI detector, arbitrary colors are again used for different channels to keep them separated. The front side Si detector and the CsI waveforms are inverted in polarity while the rest of the waveforms are normal polarity.

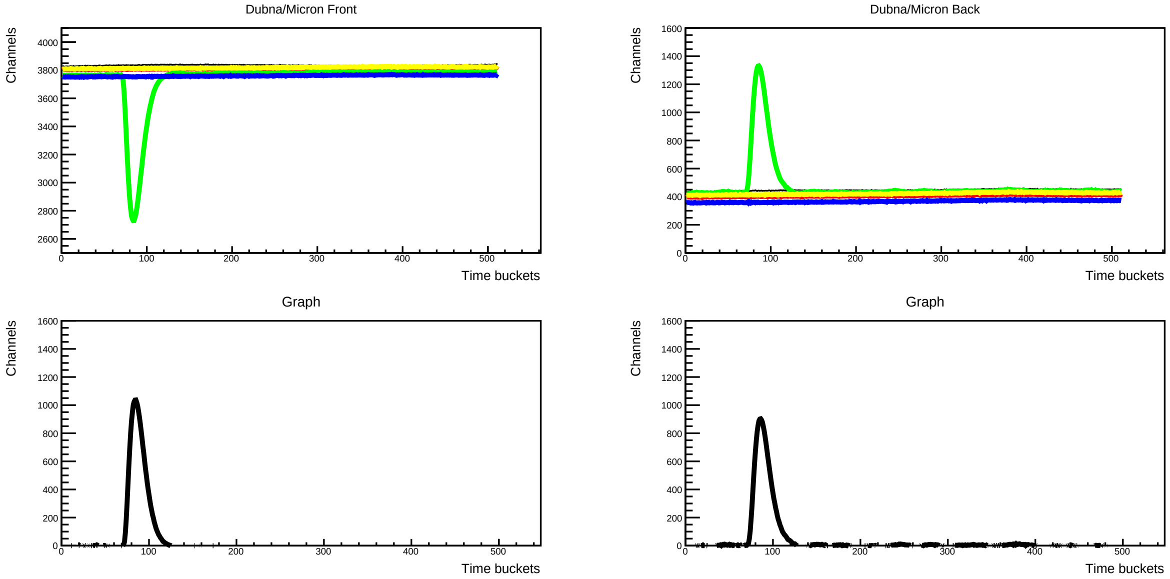

Figure 4.17: Top: raw waveforms with FPN channels for the front (left) and back (right) of a Si detector. Bottom: Fully processed waveforms with polarity correction for the front (left), FPN channel subtraction, and baseline subtraction.

To extract the energy and timing information from the waveforms a fitting procedure was utilized. Shapers, ideally, create waveforms that approximate a Gaussian. In reality, however, shaper signals are not Gaussian and are instead defined by the following function.

$$c_0 + xc_1 + (x \geq c_2) * c_4 \left(\frac{x - c_2}{c_3}\right)^{c_4} \mathrm{e}^{c_5 \frac{x-c_2}{c_3}} \sin\left(\frac{x - c_2}{c_3}\right) \tag{4.1}$$

This function is for a waveform that starts at $x = c_2$ with a linear background defined by c_0 and c_1. Parameters c_4 and c_5 are ideally the same value and represent the order of the RC circuit that is used for shaping. For the AGET shaper the parameters c_4 and c_5 should be 3, however no shaper is exactly ideal and c_4 was allowed to vary between 2 and 4. For the Mesytec shaper the circuit used is a 5^{th} order CR-RC^5 filter so c_4 and c_5 should be 5. As with the AGET shaper the Mesytec shaper is not ideal and c_4 was allowed to vary.

After fitting the waveform, the linear parameters are set to zero, effectively subtracting any remaining linear background. The energy is defined by the maximum of the function. The timing is defined as a constant fraction of the maximum, the time where the function has a value of 15% of the maximum. An advantage of fitting the waveforms is the timing information can be determined consistently.

Fitting the waveforms for the CsI detectors and the side strips and chains was a necessity. For the CsI detectors the gain was set to be sensitive to low energy signals for particles with less than 1 MeV; the consequence of this was a significant portion of the CsI waveforms were very saturated. By fitting these saturated waveforms, the energy and timing information was reliably recoverable as shown in Figure 4.18.

As noted above the side regions of the TexAT Micromegas use a strip and chain arrangement. The strips and chains form pads with effectively large active areas compared to the central region pads. It was common for signals in the central region from the beam or heavy recoil particles to induce an inverted signal on the strip and chains. To remove this induced signal the waveforms for the strips and chains were fit with a function that was the sum of an inverted waveform and an non-inverted waveform as shown in Figure 4.19. The parameters of the inverted waveform were

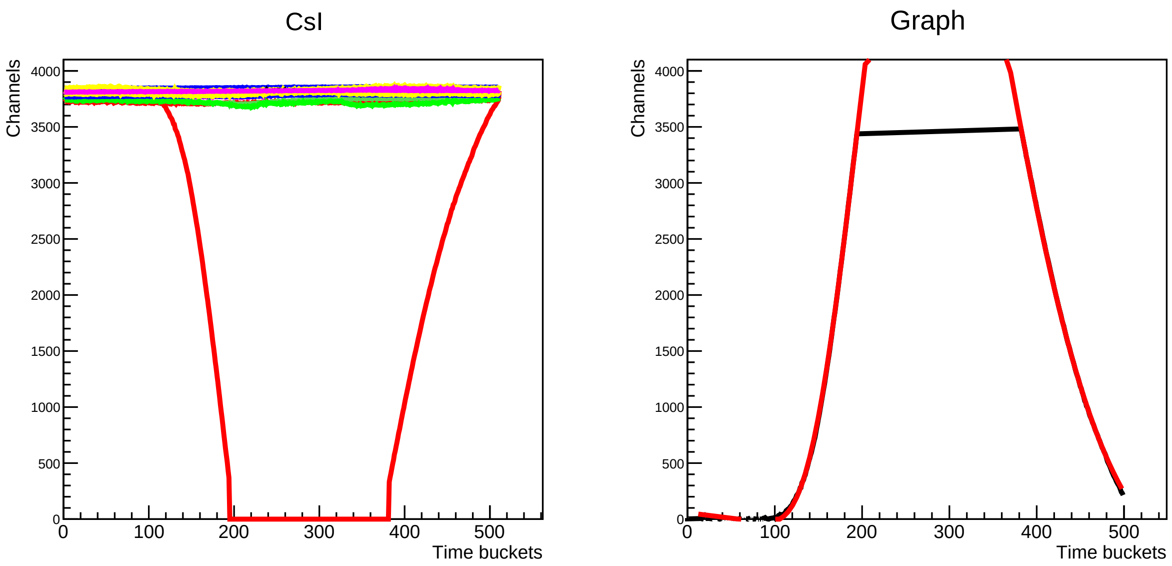

Figure 4.18: Left: Raw, saturated CsI waveform with FPN channels. Right: Processed waveform with the waveform fit. The saturation is shown as a roughly horizontal line in the processed waveform.

defined by the parameters of the waveform fit done to the central region waveforms, with c_4 fixed to being negative and allowed to otherwise vary freely as the magnitude of the inverted waveform was smaller than the signals that induced it. The true strip or chain waveform was, thus, defined by the parameters of the non-inverted waveform.

4.4.3 Track Reconstruction

The process of reconstructing tracks in the TexAT TPC starts with "cleaning" the tracks in the side strip and chain regions. With the strip and chain configuration it is known which strips and chains particles passed through, but not the trajectory they followed. To obtain the trajectory the timing of the signal in the strips and chains is compared by looping over all chains for each strip and recording which chain had the smallest timing difference for each strip. Using this timing comparison a "cleaned" track is acquired as seen in the before and after in Figure 4.20.

The next step of track reconstruction is to fit the tracks in 3D with lines for the light recoil, beam, and heavy recoil. For this experiment the track of the heavy recoil did not deviate far from the beam, making it impossible to resolve clearly so the fitting was done in two regions: low gain

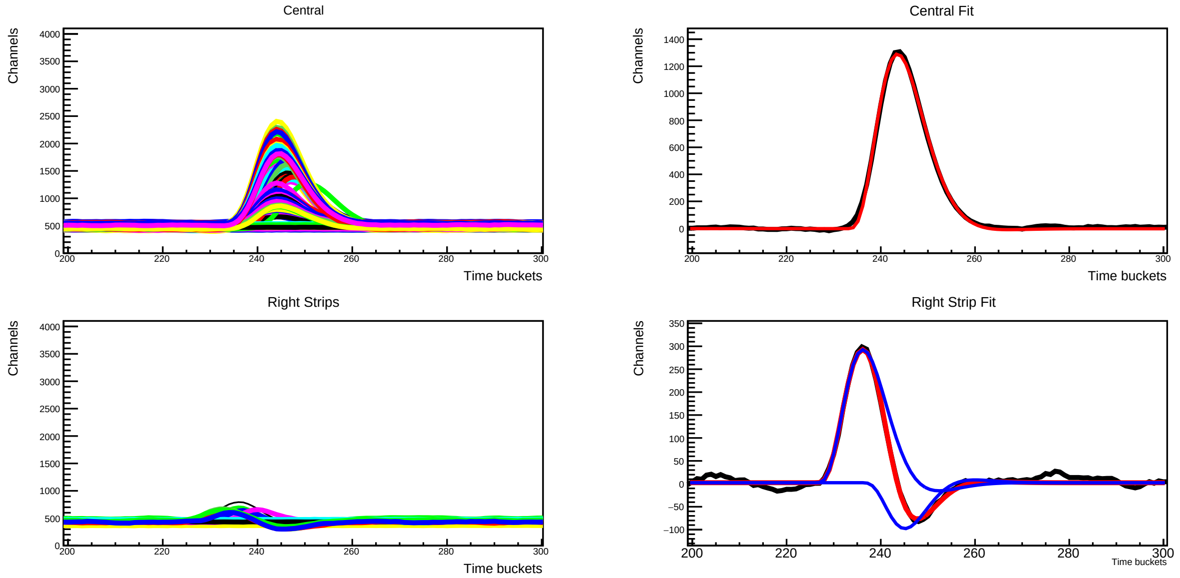

Figure 4.19: Top left: Raw waveforms for the central region of the Micromegas with FPN channels. Top right: Processed waveform for one channel in the central region with the fit drawn in red. Bottom left: Raw waveforms for the right side strips and the FPN channels. Bottom right: Processed waveform for one strip with the waveform fit in red and the two waveform components of the fit in blue.

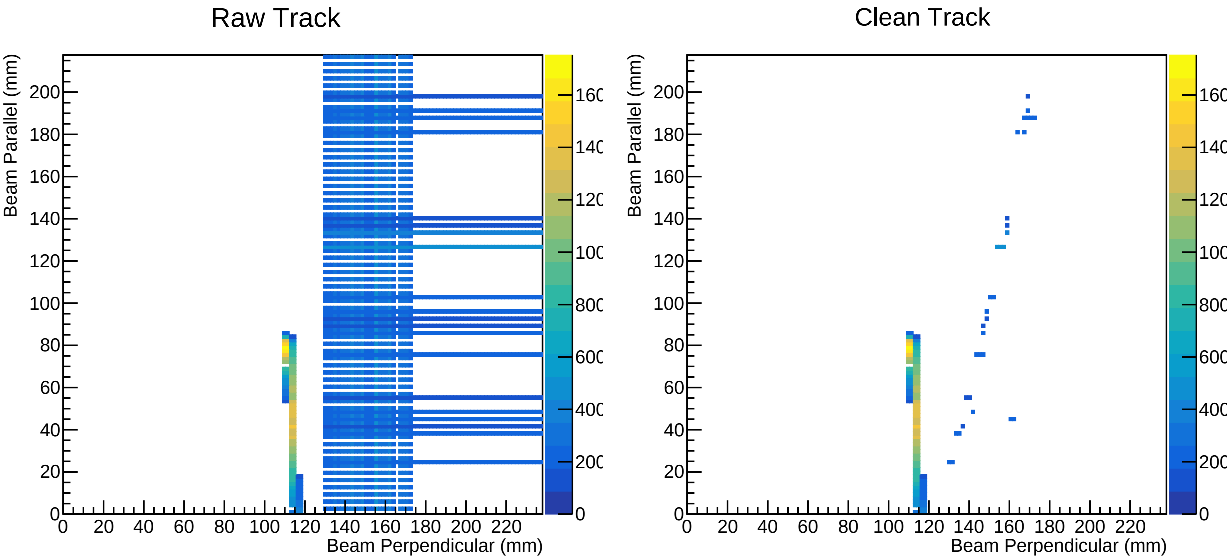

Figure 4.20: The effect of track cleaning using timing is shown on the right with the raw strip and chain information on the left. For the raw track on the left the energy of each micromegas pad is plotted as a function of position. The cleaned track plots the same but the position of the energy recorded in the strips and chains is localized to the positions where the timing is the same.

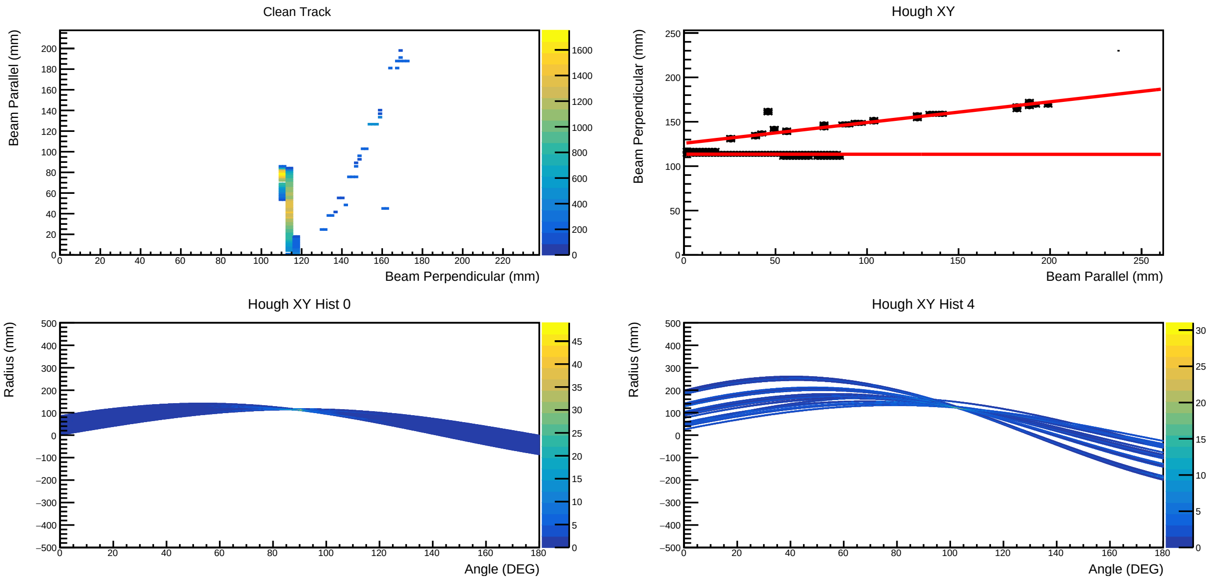

Figure 4.21: Top left: A cleaned track for an event. Top right: The result of the Hough transform on the track. The Hough transform does not do well for lines nearly parallel to the y-axis so the axis are flipped before applying the Hough transform. Bottom left: The Hough transform for the high-gain region.. Bottom right: The Hough transform for the low-gain region.

and high gain. The low gain region was defined by the first 7/8 of the central region where the beam and heavy recoil were restricted. The high gain region was defined as the side regions and the last 1/8th of the central region where the gain was sufficient to detect light recoil particles.

To obtain the fits, rather than fitting with a linear function, the Hough Transform was utilized [51]. The Hough Transform draws a line from an arbitrary origin then another line perpendicular to this line that intersects a chosen data point. The distance from the origin to this second line, hereafter referred to as the radius, and the angle of the first line are the values of interest. By varying the angle through half a circle and performing the procedure for every data point a plot of radius vs angle for every data point can be obtained. Anywhere on this plot where several data points give the same radius and angle represents a line made by those data points.

The Hough transform is used in this experiment by varying the angle in 0.1° increments from 0° to 180°. The results of the transform for each data point in a region are stored in a 2D histogram and the bin with the highest number of counts is selected as the radius and angle defining the line

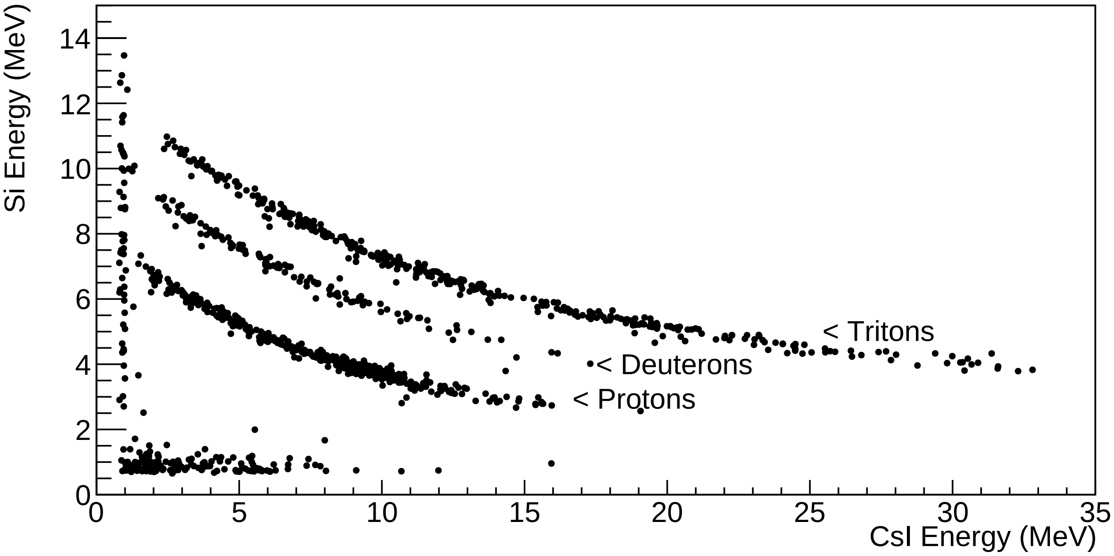

Figure 4.22: The energy deposited in the Si detectors vs the CsI detectors for the 600 μm Si detectors. Protons, deuterons and tritons can be clearly seen as labeled.

perpendicular to the line of interest as seen in the lower plots of Figure 4.21, the upper right plot shows the lines found by the Hough transform. Figure 4.21 shows an advantage of the Hough transform over a linear fit, the result of the Hough transform is unaffected by outlier points. This procedure is done for the plane parallel to the Micromegas (x, y), the plane perpendicular to the Micromegas but parallel to the beam axis (y, z), and the plane perpendicular to the Micromegas and beam axis (x, z). The (x, y) and (y, z) results together define a 3D track. The position where the light recoil track in the (x, y) plane crosses the beam axis is defined as the vertex position where the reaction occurred.

4.4.4 Reaction Identification

To obtain a final excitation function, events of interest must be determined. The simplest first step is to look at the energy of the Si detectors against the energy of the CsI detectors. Any protons, deuterons, or tritons that punch through the Si detector show up on this plot as unique bands as in Figure 4.22. Another useful set of plots are ones looking at the energy of the light recoil particle in the Si+CsI telescopes against either the vertex position from track reconstruction or the stopping

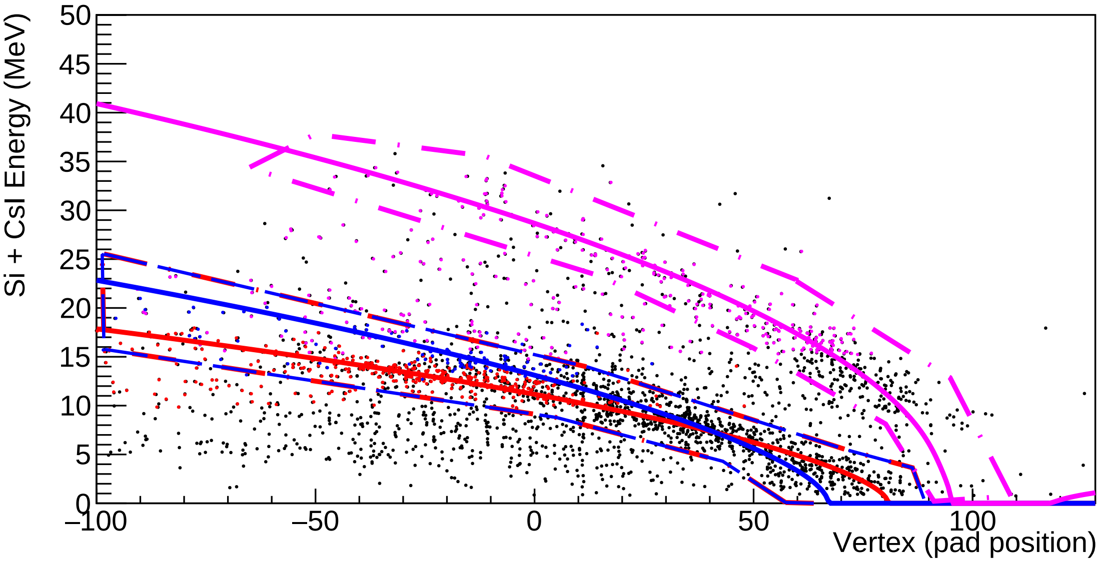

Figure 4.23: Plot of the location in the TPC of the reconstructed vertex vs the energy in the Si+CsI telescopes for the Dubna detectors. The red points are protons, the blue are deuterons, and the magenta are tritons as identified by the Si vs CsI plot. The red and blue dashed line is the graphical cut on ^{12}Be(p,p) and ^{12}Be(p,d) events while the magenta dashed line is the graphical cut on ^{12}Be(p,t) events. The red, blue, and magenta lines are the calculations based on kinematics and energy loss in the gas for the reactions.

position along the beam axis of the heavy recoil particle. An energy vs vertex plot is shown in Figure 4.23 and an energy vs endpoint plot is shown in Figure 4.24. The endpoint is much more cleanly-defined than the vertex position and was used as the primary method for reaction identification. The procedures described above were shown to reliably identify events related to ^{12}Be(p,p)^{12}Be elastic scattering, with one notable exception. As can be seen in Figure 4.24 the ^{12}Be(p,p)^{12}Be and ^{12}Be(p,d)^{11}Be(g.s.) reactions (red and blue dots) become kinematically too close at lower energies and cannot be separated. As a result, deuterons from the ^{12}Be(p,d)^{11}Be(g.s.) reaction represent a small but not negligible background and have to be subtracted as explained below.

To further clean the events, the energy deposited in the Micromegas was compared to the energy of the Si+CsI telescopes and the $Z = 1$ band could be selected on as shown in Figure 4.25. The gain on the micromegas was limited by the gas pressure and the physical limitations of the

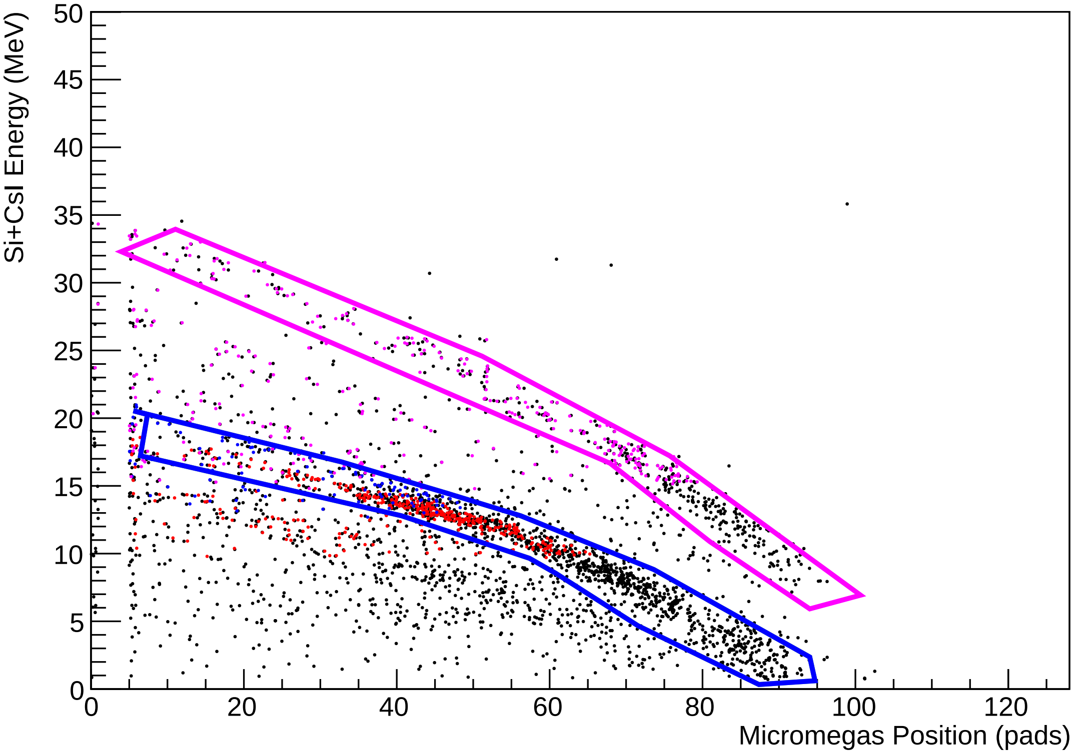

Figure 4.24: Plot of the location in the TPC where the heavy recoil track ends vs the energy in the Si+CsI telescopes for the Dubna detectors. The red points are protons, the blue are deuterons, and the magenta are tritons as identified by the Si vs CsI plot. The red and blue line is the graphical cut on ^{12}Be(p,p) and ^{12}Be(p,d) events while the magenta line is the graphical cut on ^{12}Be(p,t) events.

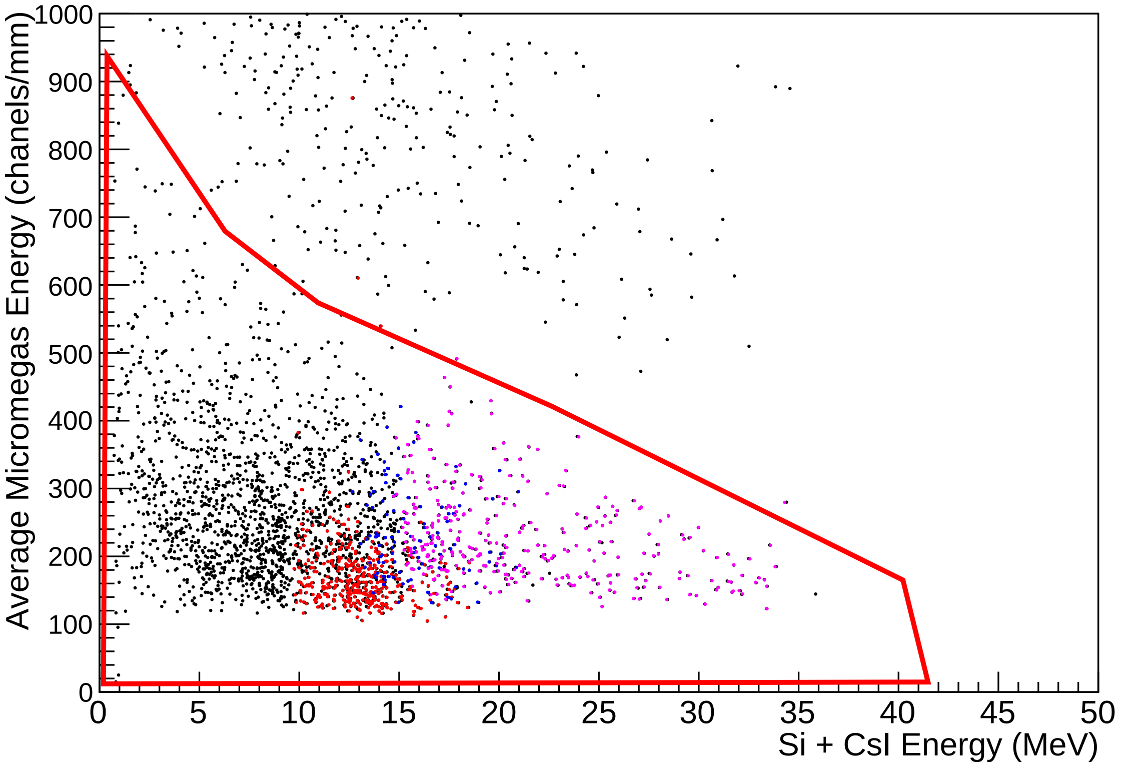

Figure 4.25: Plot of energy in the Si+CsI telescopes for the Dubna detectors vs the average energy in the micromegas strips. The red points are protons, the blue are deuterons, and the magenta are tritons as identified by the Si vs CsI plot. The red line is the cut around Z=1 particles.

strength of the potential fields in the micromegas and GEM. Because of the limited gain in the micromegas it was impossible to separate protons from deuterons and tritons using this method as can be seen by the poor p, d, and t separation in Figure 4.25.

Due to the inability to separate protons and deuterons at low energies, the ^{12}Be(p,p) and ^{12}Be(p,d)^{11}Be(g.s.) reactions had to be handled together. The total counts of the mixed (p,p) and (p,d) reactions is shown in Figure 4.26. To adjust the counts for the (p,d) reaction the cross section for the (p,d) reaction was assumed to be mostly flat. To obtain the yield of deuterons from the (p,d) reaction at all energies, we used the measured deuteron yields at higher energies and extrapolated to lower energies. More specifically, the yield for the (p,d) reaction was obtained by normalizing the counts by the solid angle and effective target thickness for each energy bin and

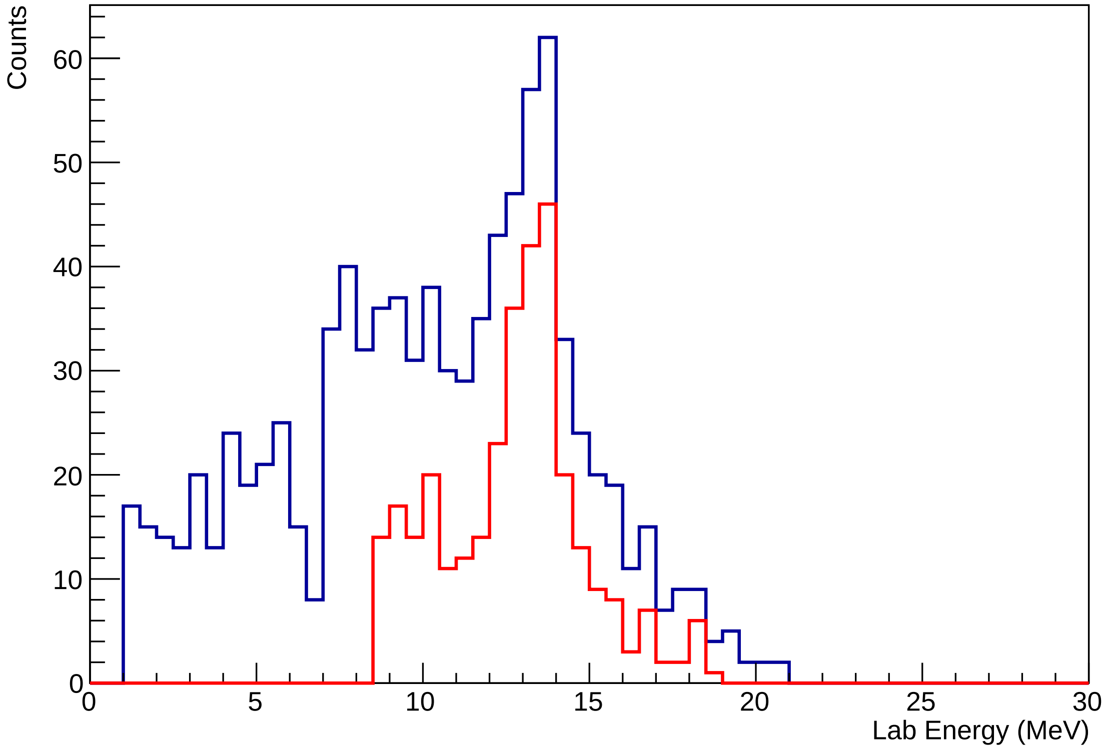

Figure 4.26: Total counts in the lab frame for the 0° detector. The red is events identified as (p,p) from the Si vs CsI plot while the dark blue is (p,p) and (p,d) events.

fitting the higher energy data with the following function:

$$y(x) = \frac{c_0}{1 + \mathrm{e}^{\frac{x-c_1}{c_2}}} \tag{4.2}$$

The results of this fit are seen in Figure 4.27. The background from deuterons, represented by the red curve, was subtracted from the combined ^{12}Be(p,p)^{12}Be(g.s.) and ^{12}Be(p,d)^{11}Be(g.s.) spectrum. Figure 4.28 shows the result of this subtraction (blue histogram), compared to the clean, background-free ^{12}Be(p,p)^{12}Be spectrum at higher energies (red histogram). The final ^{12}Be(p,p)^{12}Be(g.s.) excitation function obtained this way is shown in Figure 4.29 (lab frame) and Figure 4.30 (c.m. frame).

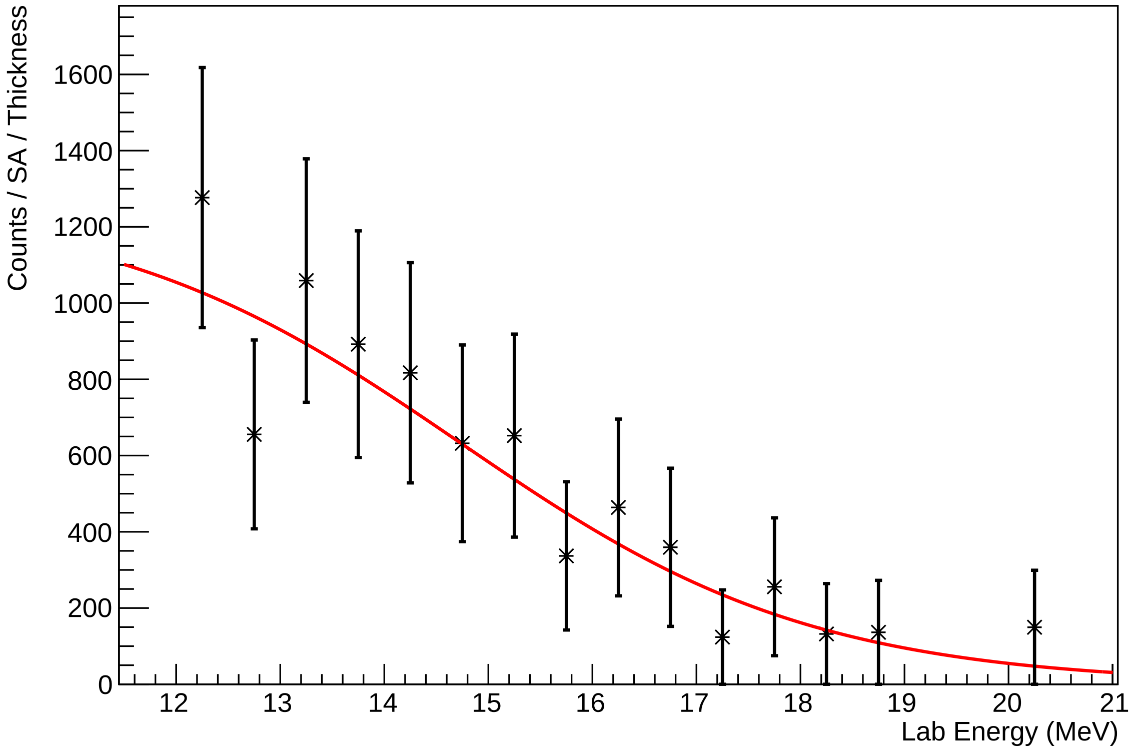

Figure 4.27: A plot of the counts / solid angle / target thickness for a given energy bin in the lab frame for ^{12}Be(p,d) events for the $0°$ detector. The fit of Equation 4.2 is plotted in red and was used to estimate the total counts in the mixed spectra associated with the ^{12}Be(p,d) reaction.

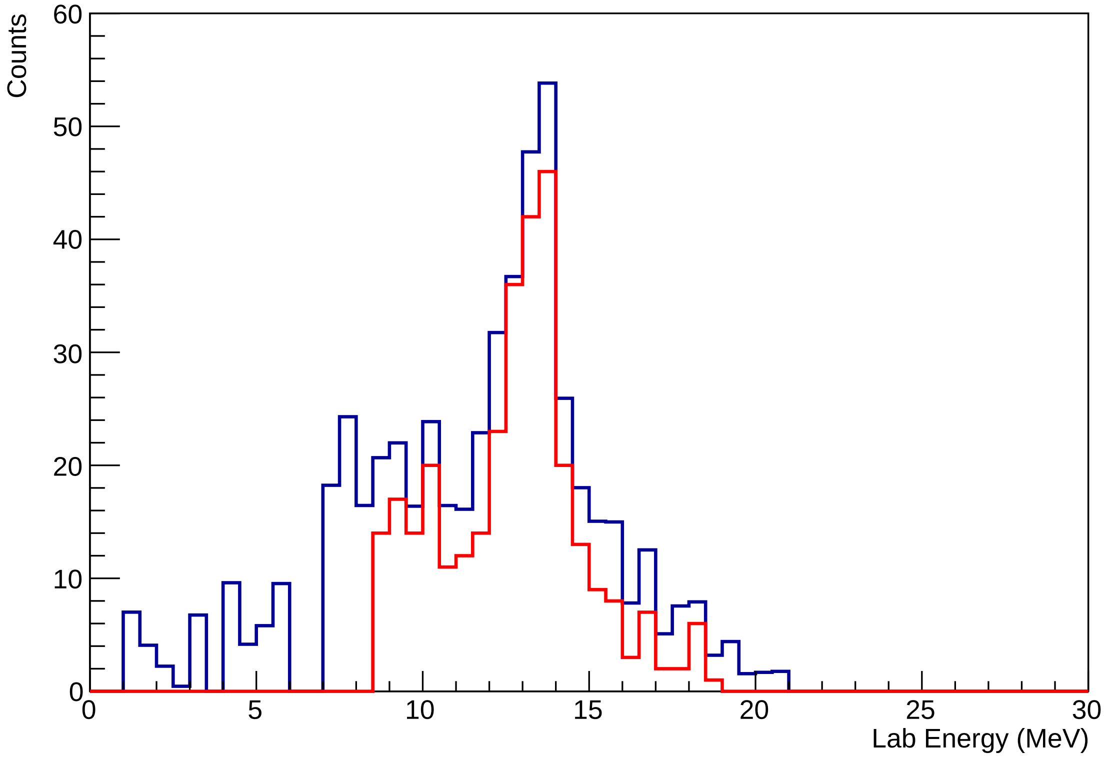

Figure 4.28: Total counts in the lab frame for the 0° detector corrected for the (p,d) as detailed in the text. The red is events identified as (p,p) from the Si vs CsI plot while the dark blue is (p,p) and (p,d) events with the (p,d) counts removed using the fitting method.

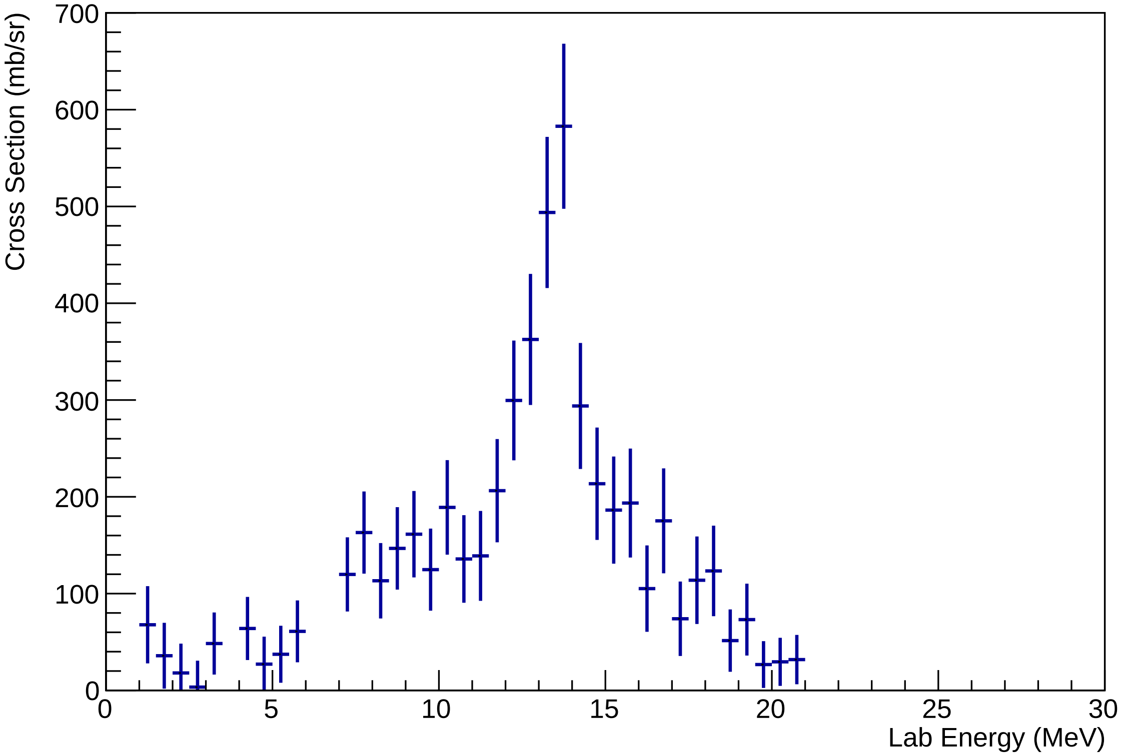

Figure 4.29: The final cross section for ^{12}Be(p,p) in the lab frame for the 0° detector.

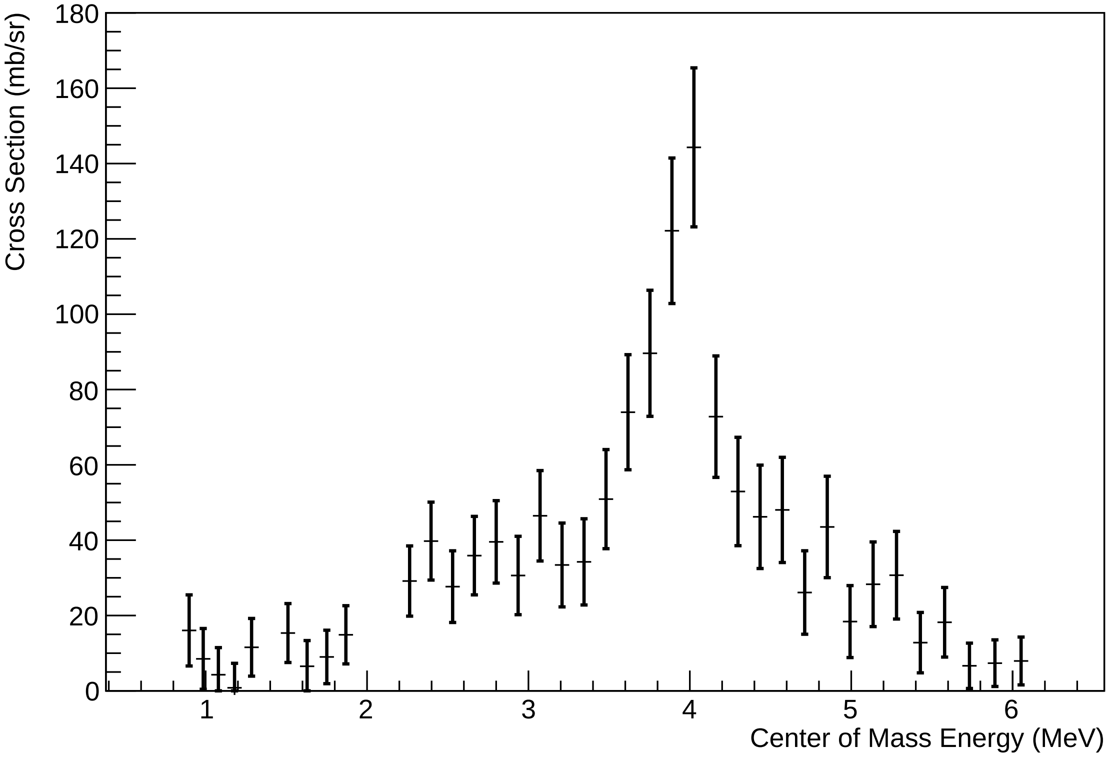

Figure 4.30: The final cross section for ^{12}Be(p,p) in the center of mass frame for the $0°$ detector.

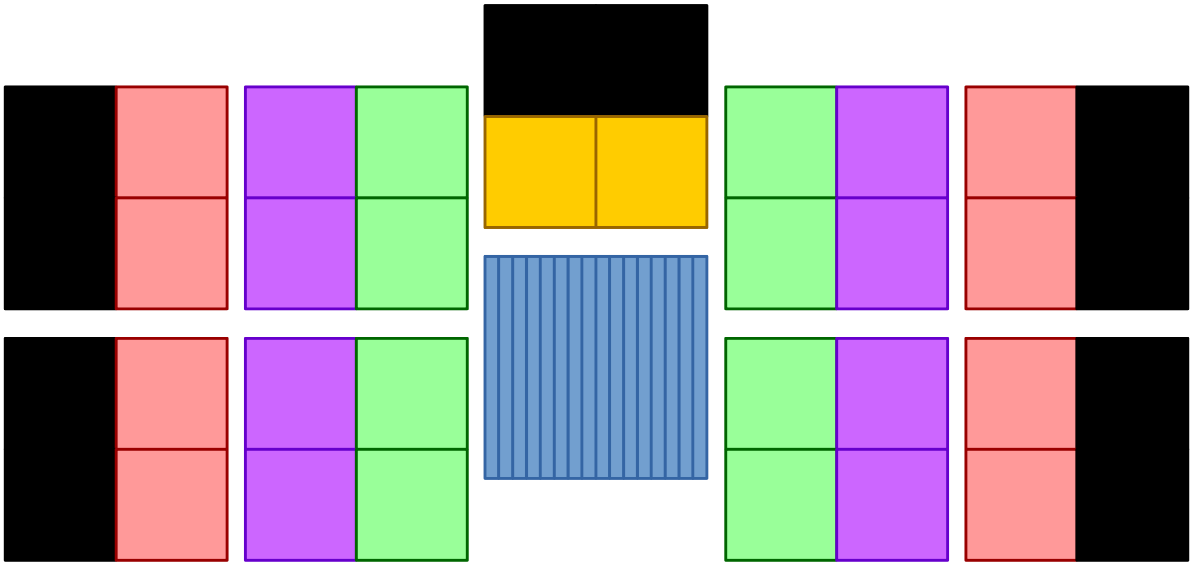

Figure 4.31: Diagram of how parts of the Si detector wall were grouped for analysis. The divisions are the 0° detector, the bottom two quadrants of the detector above that detector, and the vertical pairs of quadrants for the rest of the detectors.

4.5 Results

For the analysis the segmentation of the Si detectors was used to group events as seen in Figure 4.31. The four quadrant detectors on the sides were grouped together by the vertical quadrants while the 0° detector was used in its entirety. The top quadrants of the detector above the 0° were omitted due to being mostly blocked by the TPC. The outer quadrants of the outer detectors were omitted due to being partially shadowed by the TPC frame. These groupings allow for the excitation function to be measured at a range of angles. Due to the energy loss of the beam there is a correlation between excitation energy and angle for each grouping, with higher energy in the center of mass corresponding to a larger angle in center of mass and lower energy corresponding to a smaller center of mass angle. The angle correlation was done by energy bin as the average angle measurable for the segmentation grouping from the position in the TPC the energy bin corresponds to. This means that the average angle for the central detector (blue in Figure 4.31) at 4 MeV in the

Table 4.1: Best fit R-matrix parameters for the T=5/2 states in ^{13}B with channel radius of 4.2 fm and γ_{sp}^2=2.55 MeV. E$_{ex}$ is an excitation energy in ^{13}B, E$_{cm}$ is the center of mass energy, Γ is a total width, Γ_p and Γ_n are the proton and neutron partial widths respectively, S is a spectroscopic factor, and γ_p^2 and γ_n^2 are the square of the proton and neutron reduced widths respectively.

J$^\pi$	E$_{cm}$ MeV	E$_{cm}$ MeV	Γ keV	Γ_p keV	Γ_n keV	S	γ_p^2 keV	γ_n^2 keV
$\frac{1}{2}^+$	18.22 ± 0.15	2.42 ± 0.15	660 ± 500	180	480	0.17 ± 0.13	87	350
$\frac{5}{2}^+$	19.95 ± 0.14	4.15 ± 0.14	720 ± 400	220	500	0.37 ± 0.20	190	760

center of mass will be larger than that for the inner quadrants in the side detectors (green in Figure 4.31) which will be larger than for the next set of quadrants (purple in Figure 4.31).

The excitation function for ^{12}Be+p is expected to be dominated by the $T = 5/2$ states, like the ^{8}Li+p excitation function was dominated by $T = 3/2$ states. The excitation function has been calculated using two $T = 5/2$ resonances and additional background "resonances" at high energy to account for the $T = 3/2$ continuum. The included $T = 5/2$ resonances are a 1/2$^+$ resonance with center of mass energy $E = 2.42 \pm 0.15$ MeV and a 5/2$^+$ resonance with center of mass energy $E = 4.15 \pm 0.14$ MeV. The widths were calculated from Equations 4.3-4.4 then varied to obtain the best fit. The results of this fit are shown in Figure 4.32 and the parameters and tentative results are shown in Table 4.1. The χ^2 of the fit is 2.35.

$$\gamma_p^2 = S\gamma_{sp}^2 \left(C^{2\,\frac{1}{2}\,\frac{5}{2}}_{2\,-\frac{1}{2}\,\frac{3}{2}} \right)^2 \tag{4.3}$$

$$\gamma_n^2 = S\gamma_{sp}^2 \left(C^{2\,\frac{1}{2}\,\frac{5}{2}}_{1\,\frac{1}{2}\,\frac{3}{2}} \right)^2 \tag{4.4}$$

This result is consistent with the notion that the structure of low-lying states in ^{13}Be is a 1/2$^+$ ground state with a 5/2$^+$ first excited state. There is no clear evidence for any additional states. The wavefunction of the T=5/2 states in ^{13}B is dominated by the neutron channel. The energy of the corresponding states in ^{13}Be is calculated as the energy of the states above the threshold for neutron decay to the first T=2 state in ^{12}B, 17.61 MeV. Thus, for ^{13}Be, this gives an energy for the

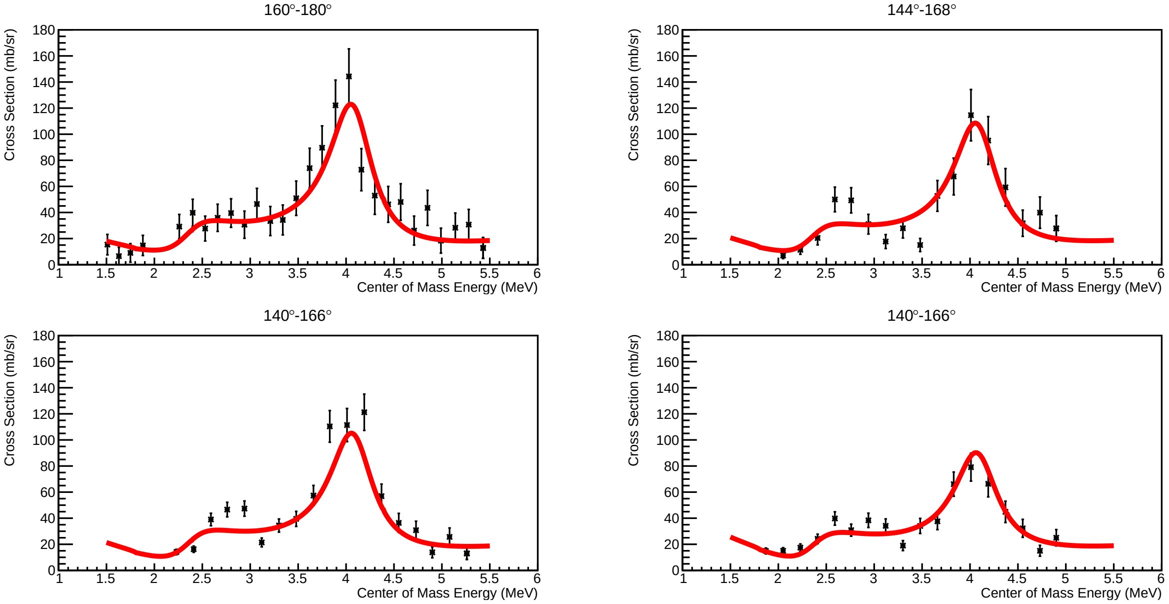

Figure 4.32: The cross section with the R-matrix calculation in red. Top left: $0°$ detector covering angles $168° - 180°$; Top right: detector above the $0°$ detector covering angles $144° - 168°$; bottom left: inner quadrants of the side Dubna detectors covering angles $140° - 166°$; bottom right: outer quadrants of the side Dubna detectors covering angles $141° - 166°$.

$1/2^+$ state as 0.61 ± 0.15 MeV above threshold and for the $5/2^+$ state as 2.34 ± 0.14 MeV above the ^{12}Be+n threshold.

In the investigation of possible ^{12}C contamination in the ^{12}Be beam, we have not observed any evidence of ^{12}C presence, which would show up as a sharp peak in the proton spectrum at a center of mass energy of 1.6 MeV due to the narrow 5/2$^+$ state in ^{13}N at that center of mass energy. Based on the fact that the maximum cross section for ^{12}C(p,p) is a factor of four larger than the measured maximum cross section for ^{12}Be(p,p) and there is no evidence for the narrow peak near 1.6 MeV (Figure 4.30), we can estimate that any ^{12}C contamination was at a level less than 1%.

4.6 Discussion

Many experimental studies of ^{13}Be have suggested a $1/2^+$ ground state near the decay threshold and a $5/2^+$ first excited state in the 2.0 - 2.4 MeV energy range [8, 9, 14]. Some theoretical studies have also suggested this configuration [16, 18]. The results here support this configuration, finding a $1/2^+$ ground state and a $5/2^+$ excited state sufficient to reproduce the excitation function measured across a number of angles and energies. The location of the $5/2^{+}$ state at 2.34 ± 0.14 MeV in ^{13}Be reported here supports recent studies identifying this state in the 2.3-2.4 MeV range [11, 12, 13, 14]. The $1/2^{+}$ ground state at 0.61 ± 0.15 MeV in ^{13}Be supports the experimental [8, 9, 10, 14, 11, 12, 13] and theoretical [16, 18] suggestions of an s-wave ground state near threshold.

The possibility of a negative parity ground state has been suggested in theoretical studies [17, 19] and some experimental studies [9]. The result of replacing the $1/2^{+}$ ground state with a $1/2^{-}$ ground state is shown is Figure 4.33. The $1/2^{-}$ ground state is unable to reproduce the measured excitation function at center of mass energies below 3.5 MeV. The negative parity ground state with a $5/2^{+}$ excited state is not supported by these results.

The peak at 4 MeV is described in the R-matrix calculation with a $5/2^{+}$ resonance. The option of a $3/2^{+}$ resonance instead was investigated and is shown in Figure 4.33 (magenta dashes). The magnitude of the cross section for the $3/2^{+}$ option does not describe the excitation function as well as the $5/2^{+}$ option, supporting the $5/2^{+}$ assignment.

There are suggestions in the literature that there is a $1/2^{-}$ state around 0.5 MeV [11] with the $1/2^{+}$ ground state below that energy. The results presented in this thesis do not support this hypothesis as the $1/2^{-}$ spin-parity assignment for a state at 0.5 MeV (2.3 MeV center of mass energy in the p+^{12}Be system) would lead to a strong dip at that energy, which is not observed experimentally (Figure 4.33). Attempts to introduce the $1/2^{-}$ state at 0.8 MeV, suggested in Reference [10], always lead to a worse agreement of the fit with the experimental data. The T=5/2 $1/2^{-}$ at 0.8 MeV (2.6 MeV in c.m. for the p+^{12}Be system) would have to be significantly narrower than our experimental resolution (50 keV in center of mass) to escape observation. This means that the ^{12}Be(g.s.)+n spectroscopic factor for this hypothetical $1/2^{-}$ state at 0.8 MeV would have to be on the order of 0.01 or below to not show up in the observed spectrum of IAS in ^{13}B.

4.7 Conclusion

The structure of low-lying states in ^{13}Be is a topic of great interest and much debate. Experimental and theoretical studies have thus far been unable to make definitive conclusions about the

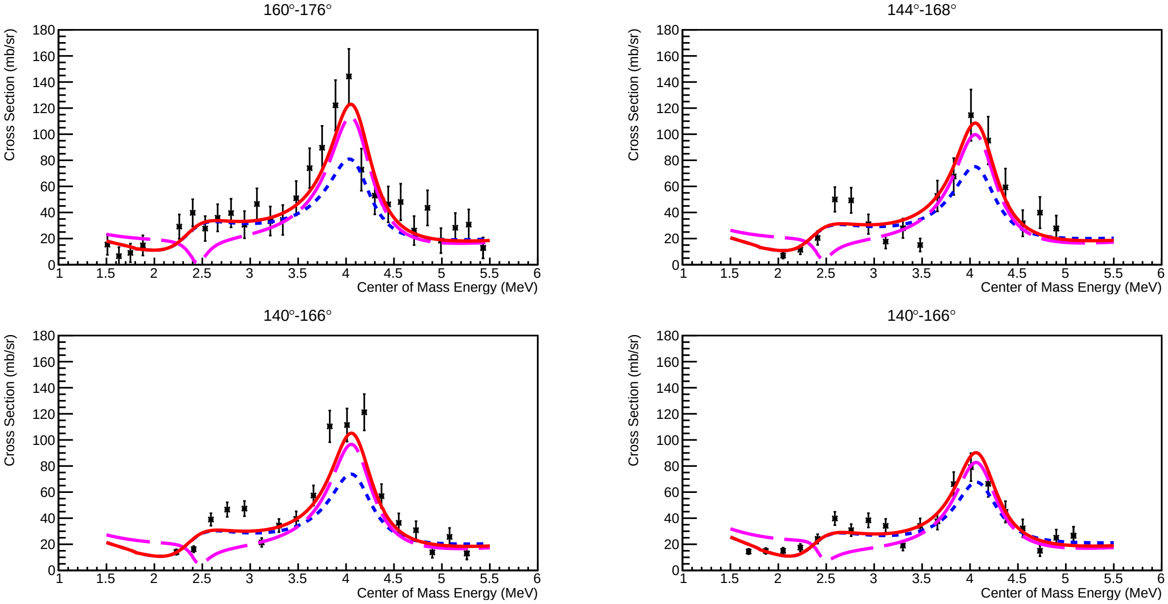

Figure 4.33: The cross section with the R-matrix fit in red, the calculation for a negative parity ground state in blue dots, and a 3/2$^+$ first excited state in magenta dashes. Top left: $0°$ detector covering angles $168° - 176°$; Top right: detector above the $0°$ detector covering angles $144° - 168°$; bottom left: inner quadrants of the side Dubna detectors covering angles $140° - 166°$; bottom right: outer quadrants of the side Dubna detectors covering angles $141° - 166°$.

structure of this nucleus. By studying the isobaric analogue of ^{13}B with TexAT in inverse kinematics using ^{12}Be+p it has been shown that the excitation function can be reproduced well with an R-matrix calculation using only a 1/2$^+$ resonance and a higher energy 5/2$^+$ resonance. The structure of the low-lying states in ^{13}Be is reported as a $1/2^+$ ground state at 0.61 ± 0.15 MeV and a $5/2^+$ excited state at 2.34 ± 0.14 MeV above the ^{12}Be+n threshold, which are consistent with several experimental and theoretical studies. A negative parity ground state is not supported, as suggested in some studies [9, 17, 19], nor are claims of a negative parity state at 0.5 MeV or 0.8 MeV unless that state has a rather small spectroscopic factor (0.01 or less). If the latter is true then we may miss this state due to finite energy resolution (50 keV) and limited statistics.

5. CONCLUSION

The study of the structure of exotic nuclei is of great interest to the development of *ab initio* methods and the understanding of nuclear interactions. It has been demonstrated in this thesis that neutron rich nuclei can be studied efficiently via their isobaric analogue states in less exotic nuclei by performing resonance elastic scattering of radioactive beams on proton targets. This technique has several advantages, which include a well understood reaction mechanism, allowing for the application of the R-matrix approach, resulting in reliable spin-parity assignments. It can also be used with the Thick Target Inverse Kinematics technique, augmented by modern active target detectors, improving efficiency, energy resolution, and specificity. This method allows studying neutron rich nuclei with resonant scattering, allowing for the use of R-matrix analysis. This method was benchmarked using the A=9, T=3/2 system and then applied to establish the low-lying structure of ^{13}Be.

In the study of the A=9, T=3/2 isobaric quartet through ^{8}Li+p resonant scattering, the effectiveness of the method of using resonant scattering to populate the high-isospin states was tested. The excitation function for resonant elastic scattering populating states in ^{9}Be was dominated by the high isospin, T=3/2, states. This allowed for the R-matrix method to be applied to the T=3/2 states of interest. The results of the R-matrix analysis reproduced the excitation function very well using parameters calculated from knowledge of ^{9}Be as well as its isobaric analogues, ^{9}Li and ^{9}C. Additionally the 5/2^{+} state previously observed in ^{9}C was also identified in ^{9}Be for the first time, identifying the onset of the 2s$_{1/2}$ shell for T=3/2 states in ^{9}Be.

The low-lying structure of the unbound nucleus ^{13}Be was an open and hotly debated question, with no consensus on the level structure from experimental or theoretical studies. The spectrum of the T=5/2 isobaric analogue states in ^{13}B, established in this work for the first time, clearly indicates that the ^{13}Be ground state is 1/2^{+} and unbound by 0.6 MeV, and the 2.3 MeV resonance is a 5/2^{+} excited state. No other states are necessary to reproduce the data.

The experimental method developed and benchmarked in this thesis can now be utilized for spectroscopy of many other neutron-rich nuclei. An example of applying this method would be populating states in the isobaric analogue of ^{10}Li, ^{10}Be, through the ^{9}Li(p,p) reaction which has been performed at Texas A&M University Cyclotron Institute with analysis ongoing. Another example of a study where this method could be applied is the structure of low-lying unbound states in ^{21}O through the ^{20}O(p,p) resonance scattering reaction populating analogous states in ^{21}F.

REFERENCES

[1] G. V. Rogachev, E. D. Johnson, J. Mitchell, V. Z. Goldberg, K. W. Kemper, and I. Wiedenhöver *AIP Conf. Proc.*, vol. 1213, p. 137, 2010.

[2] I. Wiedenhöver, L. T. Baby, D. Santiago-Gonzalez, A. Rojas, J. C. Blackmon, G. V. Rogachev, J. Belarge, E. Koshchiy, A. N. Kuchera, L. E. Linhardt, J. Lai, K. T. Macron, M. Matos, and B. C. Rascol *Proceedings of the 5th International Conference on "Fission and properties of neutron-rich nuclei" (ICFN5)*, pp. 144–151, 2014.

[3] A. M. Lane and R. G. Thomas, "R-matrix theory of nuclear reactions," *Rev. Mod. Phys.*, vol. 30, pp. 257–353, Apr 1958.

[4] A. H. Wuosmaa, K. E. Rehm, J. P. Greene, D. J. Henderson, R. V. F. Janssens, C. L. Jiang, L. Jisonna, E. F. Moore, R. C. Pardo, M. Paul, D. Peterson, S. C. Pieper, G. Savard, J. P. Schiffer, R. E. Segel, S. Sinha, X. Tang, and R. B. Wiringa, "Neutron spectroscopic factors in $^9\mathrm{Li}$ from $^2\mathrm{H}(^8\mathrm{Li}, p)^9\mathrm{Li}$," *Phys. Rev. Lett.*, vol. 94, p. 082502, Mar 2005.

[5] J. Hooker, G. V. Rogachev, E. Koshchiy, S. Ahn, M. Barbui, V. Z. Goldberg, C. Hunt, H. Jayatissa, E. C. Pollacco, B. T. Roeder, A. Saastamoinen, and S. Upadhyayula, "Structure of $^9\mathrm{C}$ through proton resonance scattering with the texas active target detector," *Phys. Rev. C*, vol. 100, p. 054618, Nov 2019.

[6] C. Hunt, G. V. Rogachev, S. Almaraz-Calderon, A. Aprahamian, M. Avila, L. T. Baby, B. Bucher, V. Z. Goldberg, E. D. Johnson, K. W. Kemper, A. N. Kuchera, W. P. Tan, and I. Wiedenhöver, "Observation of $t = 3/2$ isobaric analog states in $^9\mathrm{Be}$ using $p\ +^8$ Li resonance scattering," *Phys. Rev. C*, vol. 102, p. 014615, Jul 2020.

[7] A. N. Ostrowski *et al. Zeitschrift für Physik A Hadrons and Nuclei*, vol. 343, pp. 489–490, Dec 1992.

[8] A. Belozyorov, R. Kalpakchieva, Y. Penionzhkevich, Z. Dlouhý, S. Piskor, J. Vincour, H. Bohlen, M. von Lucke-Petsch, A. Ostrowski, D. Alexandrov, E. Nikolskii, B. Novatskii, and D. Stepanov, "Spectroscopy of 13be," *Nuclear Physics A*, vol. 636, no. 4, pp. 419–426, 1998.

[9] M. Thoennessen, S. Yokoyama, and P. G. Hansen *Phys. Rev. C*, vol. 63, p. 014308, Dec 2000.

[10] H. Simon, M. Meister, T. Aumann, M. Borge, L. Chulkov, U. Datta Pramanik, T. Elze, H. Emling, C. Forssén, H. Geissel, M. Hellström, B. Jonson, J. Kratz, R. Kulessa, Y. Leifels, K. Markenroth, G. Münzenberg, F. Nickel, T. Nilsson, G. Nyman, A. Richter, K. Riisager, C. Scheidenberger, G. Schrieder, O. Tengblad, and M. Zhukov, "Systematic investigation of the drip-line nuclei 11li and 14be and their unbound subsystems 10li and 13be," *Nuclear Physics A*, vol. 791, no. 3, pp. 267–302, 2007.

[11] Y. Kondo, T. Nakamura, Y. Satou, T. Matsumoto, N. Aoi, N. Endo, N. Fukuda, T. Gomi, Y. Hashimoto, M. Ishihara, S. Kawai, M. Kitayama, T. Kobayashi, Y. Matsuda, N. Matsui, T. Motobayashi, T. Nakabayashi, T. Okumura, H. Ong, T. Onishi, K. Ogata, H. Otsu, H. Sakurai, S. Shimoura, M. Shinohara, T. Sugimoto, S. Takeuchi, M. Tamaki, Y. Togano, and Y. Yanagisawa, "Low-lying intruder state of the unbound nucleus 13be," *Physics Letters B*, vol. 690, no. 3, pp. 245–249, 2010.

[12] Y. Aksyutina, T. Aumann, K. Boretzky, M. J. G. Borge, C. Caesar, A. Chatillon, L. V. Chulkov, D. Cortina-Gil, U. Datta Pramanik, H. Emling, H. O. U. Fynbo, H. Geissel, G. Ickert, H. T. Johansson, B. Jonson, R. Kulessa, C. Langer, T. LeBleis, K. Mahata, G. Münzenberg, T. Nilsson, G. Nyman, R. Palit, S. Paschalis, W. Prokopowicz, R. Reifarth, D. Rossi, A. Richter, K. Riisager, G. Schrieder, H. Simon, K. Sümmerer, O. Tengblad, H. Weick, and M. V. Zhukov, "Structure of the unbound nucleus ^{13}be: One-neutron knockout reaction data from ^{14}be analyzed in a holistic approach," *Phys. Rev. C*, vol. 87, p. 064316, Jun 2013.

[13] G. Randisi, A. Leprince, H. Al Falou, N. A. Orr, F. M. Marqués, N. L. Achouri, J.-C. Angélique, N. Ashwood, B. Bastin, T. Bloxham, B. A. Brown, W. N. Catford, N. Curtis,

F. Delaunay, M. Freer, E. de Góes Brennand, P. Haigh, F. Hanappe, C. Harlin, B. Laurent, J.-L. Lecouey, A. Ninane, N. Patterson, D. Price, L. Stuttgé, and J. S. Thomas, "Structure of ^{13}be probed via secondary-beam reactions," *Phys. Rev. C*, vol. 89, p. 034320, Mar 2014.

[14] B. R. Marks, P. A. DeYoung, J. K. Smith, T. Baumann, J. Brown, N. Frank, J. Hinnefeld, M. Hoffman, M. D. Jones, Z. Kohley, A. N. Kuchera, B. Luther, A. Spyrou, S. Stephenson, C. Sullivan, M. Thoennessen, N. Viscariello, and S. J. Williams, "Population of $^{13}\mathrm{Be}$ in a nucleon exchange reaction," *Phys. Rev. C*, vol. 92, p. 054320, Nov 2015.

[15] N. Poppelier, L. Wood, and P. Glaudemans, "Properties of exotic p-shell nuclei," *Physics Letters B*, vol. 157, no. 2, pp. 120–122, 1985.

[16] P. Descouvemont, "Halo structure of $^{14}\mathrm{Be}$ in a microscopic $^{12}\mathrm{Be}$+n+n cluster model," *Phys. Rev. C*, vol. 52, pp. 704–710, Aug 1995.

[17] M. Labiche, F. M. Marqués, O. Sorlin, and N. Vinh Mau, "Structure of $^{13}\mathrm{Be}$ and $^{14}\mathrm{Be}$," *Phys. Rev. C*, vol. 60, p. 027303, Jul 1999.

[18] T. Tarutina, I. Thompson, and J. Tostevin, "Study of 14be with core excitation," *Nuclear Physics A*, vol. 733, no. 1, pp. 53–66, 2004.

[19] G. Blanchon, N. V. Mau, A. Bonaccorso, M. Dupuis, and N. Pillet, "Particle-particle random-phase approximation applied to beryllium isotopes," *Phys. Rev. C*, vol. 82, p. 034313, Sep 2010.

[20] Y. Kanada-En'yo *Phys. Rev. C*, vol. 85, p. 044320, Apr 2012.

[21] K. S. Krane, *Introductory nuclear physics*. John Wiley & Sons, 1988.

[22] J. Kelley, J. Purcell, and C. Sheu *Nuclear Physics A*, vol. 968, pp. 71 – 253, 2017.

[23] F. Ajzenberg-Selove *Nuclear Physics A*, vol. 523, no. 1, pp. 1 – 196, 1991.

[24] I. Talmi and I. Unna, "Order of levels in the shell model and spin of be^{11}," *Phys. Rev. Lett.*, vol. 4, pp. 469–470, May 1960.

[25] R. Sherr and H. T. Fortune, “Structure of $^{12}\mathrm{Be}$ and $^{12}\mathrm{O}$ ground states,” *Phys. Rev. C*, vol. 60, p. 064323, Nov 1999.

[26] B. R. Barrett, P. NavrÃątil, and J. P. Vary, “Ab initio no core shell model,” *Progress in Particle and Nuclear Physics*, vol. 69, pp. 131 – 181, 2013.

[27] J. Carlson, S. Gandolfi, F. Pederiva, S. C. Pieper, R. Schiavilla, K. E. Schmidt, and R. B. Wiringa, “Quantum monte carlo methods for nuclear physics,” *Rev. Mod. Phys.*, vol. 87, pp. 1067–1118, Sep 2015.

[28] N. Bohr, “Neutron capture and nuclear constitution,” *Nature*, vol. 137, pp. 344–348, Feb 1936.

[29] W. Hauser and H. Feshbach, “The inelastic scattering of neutrons,” *Phys. Rev.*, vol. 87, pp. 366–373, Jul 1952.

[30] G. V. Rogachev, J. J. Kolata, A. S. Volya, F. D. Becchetti, Y. Chen, P. A. DeYoung, and J. Lupton, “Spectroscopy of $^{9}\mathrm{C}$ via resonance scattering of protons on $^{8}\mathrm{B}$,” *Phys. Rev. C*, vol. 75, p. 014603, Jan 2007.

[31] V. Z. Goldberg, “Resonance scattering to study nuclei at the borders of nuclear stability,” *AIP Conference Proceedings*, vol. 455, no. 1, pp. 319–322, 1998.

[32] K. Artemov, O. P. Belyanin, A. L. Vetoshkin, R. Wolski, M. S. Golovkov, and V. Z. Goldberg *Sov. J. Nucl. Phys.*, vol. 52, p. 408, 1990.

[33] E. P. Wigner and L. Eisenbud, “Higher angular momenta and long range interaction in resonance reactions,” *Phys. Rev.*, vol. 72, pp. 29–41, Jul 1947.

[34] P. Descouvemont and D. Baye, “TheR-matrix theory,” *Reports on Progress in Physics*, vol. 73, p. 036301, feb 2010.

[35] I. J. Thompson and F. M. Nunes, *Nuclear reactions for astrophysics: principles, calculation and applications of low-energy reactions*. Cambridge University Press, 2009.

[36] D. Robson, “Theory of isobaric-spin analogue resonances,” *Phys. Rev.*, vol. 137, pp. B535–B546, Feb 1965.

[37] D. Tilley, J. Kelley, J. Godwin, D. Millener, J. Purcell, C. Sheu, and H. Weller, “Energy levels of light nuclei a=8,9,10,” *Nuclear Physics A*, vol. 745, no. 3, pp. 155–362, 2004.

[38] R. Kanungo, A. Andreyev, L. Buchmann, B. Davids, G. Hackman, D. Howell, P. Khalili, B. Mills, E. P. Rodal, S. C. Pieper, J. Pearson, C. Ruiz, G. Ruprecht, A. Shotter, I. Tanihata, C. Vockenhuber, P. Walden, and R. Wiringa, “Spectroscopic factors for the 9li ground state and n=6 shell closure,” *Physics Letters B*, vol. 660, no. 1, pp. 26 – 31, 2008.

[39] E. Tengborn, A. M. Moro, T. Nilsson, M. Alcorta, M. J. G. Borge, J. Cederkäll, C. Diget, L. M. Fraile, H. O. U. Fynbo, J. Gomez-Camacho, H. B. Jeppesen, H. T. Johansson, B. Jonson, O. S. Kirsebom, H. H. Knudsen, M. Madurga, G. Nyman, A. Richter, K. Riisager, G. Schrieder, O. Tengblad, N. Timofeyuk, M. Turrion, D. Voulot, and F. Wenander, “The ^{8}li + ^{2}h reaction studied in inverse kinematics at 3.15 mev/nucleon using the rex-isolde post-accelerator,” *Phys. Rev. C*, vol. 84, p. 064616, Dec 2011.

[40] K. W. Brown, R. J. Charity, J. M. Elson, W. Reviol, L. G. Sobotka, W. W. Buhro, Z. Chajecki, W. G. Lynch, J. Manfredi, R. Shane, R. H. Showalter, M. B. Tsang, D. Weisshaar, J. R. Winkelbauer, S. Bedoor, and A. H. Wuosmaa, “Proton-decaying states in light nuclei and the first observation of $^{17}\mathrm{Na}$,” *Phys. Rev. C*, vol. 95, p. 044326, Apr 2017.

[41] J. Pniewski, K. Garbowska-Pniewska, D. Kieczewska, D. Davis, G. Bohm, U. Krecker, A. Montwill, P. Moriarty, G. Coremans-Bertrand, J. Sacton, and M. Juri, “Final-state interactions in the decay of the hypernucleus 9li and a reappraisal of the binding energies of a=9 hypernuclei,” *Nuclear Physics A*, vol. 443, no. 4, pp. 685–690, 1985.

[42] J. M. Lombaard and E. Friedland *Z. Physik*, vol. 268, p. 713, 1974.

[43] E. D. Johnson. PhD thesis, Florida State University, 2008.

[44] J. B. Ehrman, “On the displacement of corresponding energy levels of c^{13} and n^{13},” *Phys. Rev.*, vol. 81, pp. 412–416, Feb 1951.

[45] R. B. Wiringa, S. Pastore, S. C. Pieper, and G. A. Miller *Phys. Rev. C*, vol. 88, p. 044333, Oct 2013.

[46] E. Koshchiy, G. Rogachev, E. Pollacco, S. Ahn, E. Uberseder, J. Hooker, J. Bishop, E. Aboud, M. Barbui, V. Goldberg, C. Hunt, H. Jayatissa, C. Magana, R. O'Dwyer, B. Roeder, A. Saastamoinen, and S. Upadhyayula, "Texas active target (texat) detector for experiments with rare isotope beams," *Nuclear Instruments and Methods in Physics Research Section A: Accelerators, Spectrometers, Detectors and Associated Equipment*, vol. 957, p. 163398, 2020.

[47] Y. Giomataris, P. Rebourgeard, J. Robert, and G. Charpak, "Micromegas: a high-granularity position-sensitive gaseous detector for high particle-flux environments," *Nuclear Instruments and Methods in Physics Research Section A: Accelerators, Spectrometers, Detectors and Associated Equipment*, vol. 376, no. 1, pp. 29–35, 1996.

[48] F. Sauli, "The gas electron multiplier (gem): Operating principles and applications," *Nuclear Instruments and Methods in Physics Research Section A: Accelerators, Spectrometers, Detectors and Associated Equipment*, vol. 805, pp. 2–24, 2016. Special Issue in memory of Glenn F. Knoll.

[49] E. Pollacco, G. Grinyer, F. Abu-Nimeh, T. Ahn, S. Anvar, A. Arokiaraj, Y. Ayyad, H. Baba, M. Babo, P. Baron, D. Bazin, S. Beceiro-Novo, C. Belkhiria, M. Blaizot, B. Blank, J. Bradt, G. Cardella, L. Carpenter, S. Ceruti, E. De Filippo, E. Delagnes, S. De Luca, H. De Witte, F. Druillole, B. Duclos, F. Favela, A. Fritsch, J. Giovinazzo, C. Gueye, T. Isobe, P. Hellmuth, C. Huss, B. Lachacinski, A. Laffoley, G. Lebertre, L. Legeard, W. Lynch, T. Marchi, L. Martina, C. Maugeais, W. Mittig, L. Nalpas, E. Pagano, J. Pancin, O. Poleshchuk, J. Pedroza, J. Pibernat, S. Primault, R. Raabe, B. Raine, A. Rebii, M. Renaud, T. Roger, P. Roussel-Chomaz, P. Russotto, G. Saccà, F. Saillant, P. Sizun, D. Suzuki, J. Swartz, A. Tizon, A. Trifiró, N. Usher, G. Wittwer, and J. Yang, "Get: A generic electronics system for tpcs and nuclear physics instrumentation," *Nuclear Instruments and Methods in Physics Research Section A: Accelerators, Spectrometers, Detectors and Associated Equipment*, vol. 887, pp. 81–

93, 2018.

[50] E. L. R and M. M, “The ISAC post-accelerator,” *Hyperfine Interactions*, vol. 225, no. 1-3, pp. 79–97, 2014.

[51] R. O. Duda and P. E. Hart, “Use of the hough transformation to detect lines and curves in pictures,” *Commun. ACM*, vol. 15, p. 1115, Jan. 1972.